Miner Deposita (2010) 45:735–763
DOI 10.1007/s00126-010-0298-3

ARTICLE

Genesis of sediment-hosted stratiform copper–cobalt mineralization at Luiswishi and Kamoto, Katanga Copperbelt (Democratic Republic of Congo)

Hamdy A. El Desouky · Philippe Muchez · Adrian J. Boyce · Jens Schneider · Jacques L. H. Cailteux · Stijn Dewaele · Albrecht von Quadt

Received: 30 April 2009 / Accepted: 14 June 2010 / Published online: 11 July 2010

Abstract The sediment-hosted stratiform Cu–Co mineralization of the Luiswishi and Kamoto deposits in the Katangan Copperbelt is hosted by the Neoproterozoic Mines Subgroup. Two main hypogene Cu–Co sulfide mineralization stages and associated gangue minerals (dolomite and quartz) are distinguished. The first is an early diagenetic, typical stratiform mineralization with fine-grained minerals, whereas the second is a multistage syn-orogenic stratiform to stratabound mineralization with coarse-grained minerals. For both stages, the main hypogene Cu–Co sulfide minerals are chalcopyrite, bornite, carrollite, and chalcocite. These minerals are in many places replaced by supergene sulfides (e.g., digenite and covellite), especially near the surface, and are completely oxidized in the weathered superficial zone and in surface outcrops, with malachite, heterogenite, chrysocolla, and azurite as the main oxidation products. The hypogene sulfides of the first Cu–Co stage display $\delta^{34}S$ values (−10.3‰ to +3.1‰ Vienna Canyon Diablo Troilite (V-CDT)), which partly overlap with the $\delta^{34}S$ signature of framboidal pyrites (−28.7‰ to 4.2‰ V-CDT) and have $\Delta^{34}S_{SO4\text{-}Sulfides}$ in the range of 14.4‰ to 27.8‰. This fractionation is consistent with bacterial sulfate reduction (BSR). The hypogene sulfides of the second Cu–Co stage display $\delta^{34}S$ signatures that are either similar (−13.1‰ to +5.2‰ V-CDT) to the $\delta^{34}S$ values of the sulfides of the first Cu–Co stage or comparable (+18.6‰ to +21.0‰ V-CDT) to the $\delta^{34}S$ of Neoproterozoic seawater. This indicates that the sulfides of the second stage obtained their sulfur by both remobilization from early diagenetic sulfides and from thermochemical sulfate reduction (TSR). The carbon (−9.9‰ to −1.4‰ Vienna Pee Dee Belemnite (V-PDB)) and oxygen (−14.3‰ to −7.7‰ V-PDB) isotope signatures of dolomites associated with the first Cu–Co stage are in agreement with the interpretation that these dolomites are by-products of BSR. The carbon (−8.6‰ to +0.3‰ V-PDB) and oxygen (−24.0‰ to −10.3‰ V-PDB) isotope signatures of dolomites associated with the second Cu–Co stage are mostly similar to the $\delta^{13}C$ (−7.1‰ to +1.3‰ V-PDB) and $\delta^{18}O$ (−14.5‰ to −7.2‰ V-PDB) of the host rock and of the dolomites of the first Cu–Co stage. This

Editorial handling: H. Frimmel

Electronic supplementary material The online version of this article (doi:10.1007/s00126-010-0298-3) contains supplementary material, which is available to authorized users.

H. A. El Desouky (✉) · P. Muchez · J. Schneider
Geodynamics & Geofluids Research Group, K.U.Leuven,
Celestijnenlaan 200E,
3001 Leuven, Belgium
e-mail: HamdyAhmed.ElDesouky@ees.kuleuven.be

P. Muchez
e-mail: Philippe.Muchez@ees.kuleuven.be

A. J. Boyce
Isotope Geoscience Unit, SUERC,
Rankine Avenue, East Kilbride,
Glasgow G75 0QF, UK

J. L. H. Cailteux
Département Recherche et Développement,
E.G.M.F., Groupe Forrest International,
Lubumbashi, Democratic Republic of Congo

S. Dewaele
Department of Geology and Mineralogy,
Royal Museum for Central Africa (RMCA),
Leuvensesteenweg 13,
3080 Tervuren, Belgium

A. von Quadt
Institute of Isotope Geochemistry and Mineral Resources,
Swiss Federal Institute of Technology Zurich (ETH),
Clausiusstrasse 25,
8092 Zurich, Switzerland

indicates that the dolomites of the second Cu–Co stage precipitated from a high-temperature, host rock-buffered fluid, possibly under the influence of TSR. The dolomites associated with the first Cu–Co stage are characterized by significantly radiogenic Sr isotope signatures (0.70987 to 0.73576) that show a good correspondence with the Sr isotope signatures of the granitic basement rocks at an age of ca. 816 Ma. This indicates that the mineralizing fluid of the first Cu–Co stage has most likely leached radiogenic Sr and Cu–Co metals by interaction with the underlying basement rocks and/or with arenitic sedimentary rocks derived from such a basement. In contrast, the Sr isotope signatures (0.70883 to 0.71215) of the dolomites associated with the second stage show a good correspondence with the $^{87}Sr/^{86}Sr$ ratios (0.70723 to 0.70927) of poorly mineralized/barren host rocks at ca. 590 Ma. This indicates that the fluid of the second Cu–Co stage was likely a remobilizing fluid that significantly interacted with the country rocks and possibly did not mobilize additional metals from the basement rocks.

Keywords Central African Copperbelt · D.R. Congo · Stratiform Cu–Co mineralization · Stable (S, C, O) and radiogenic (Rb–Sr) isotopes · Bacterial and thermochemical sulfate reduction

Introduction

Since the discovery of the Central African Copperbelt (CACB) in the early 1890s, both mining companies and academic researchers have paid much attention to the highly economic copper–cobalt mineralization of this ore province. These efforts have been rewarded by the discovery of up to ~200 Mt of copper if subeconomic (Cu≥1 wt.%) occurrences are included (Cailteux et al. 2005) and >8 Mt of cobalt (Misra 2000). These figures define the CACB as the largest and richest sediment-hosted stratiform copper–cobalt province in the world. The sediment-hosted stratiform copper deposits are defined as stratiform disseminated to veinlet native copper and copper sulfides in a variety of often reducing sedimentary rocks, including black shales, sandstones, and carbonates (Kirkham 1989; Hitzman et al. 2005). Hitzman et al. (2005) reviewed the sediment-hosted stratiform copper deposits and explained that they are the products of evolving basin-scale, or at least subbasin-scale, fluid flow systems and that their sulfide mineralization could form throughout the basin's evolution from early diagenesis of the host sediments to basin inversion and metamorphism.

The CACB, which straddles the border between Zambia and the Democratic Republic of Congo (DRC; Fig. 1), comprises two main parts. The Congolese part (hereafter "Katanga Copperbelt") includes deposits located at the north of the DRC–Zambia border, whereas deposits to the south of this border belong to the second part of the CACB, i.e., the Zambian Copperbelt (Figs. 1 and 2; Selley et al. 2005). The Katanga Copperbelt contributes about 54% of the total production and reserves of the entire ore province (Hitzman et al. 2005). Despite the great number of known Cu–Co deposits in the CACB, it is suspected that many others are still to be discovered. A proper understanding of their genesis is required for successful exploration. Several conflicting metallogenic models have been proposed for the origin of the supergiant Cu–Co mineralization in the CACB. Reviews of these models have been given by Sweeney et al. (1991), Sweeney and Binda (1994), Cailteux et al. (2005), Selley et al. (2005), and El Desouky et al. (2008a). These models, in a chronological order, range from epigenetic–magmatic (e.g., Bateman 1930; Davidson 1931; Gray 1932; Jackson 1932) to syn-sedimentary (e.g., Garlick 1961, 1981, 1989; Fleischer et al. 1976), early to late diagenetic (e.g., Bartholomé et al. 1972; Bartholomé 1974; Unrug 1988; Annels 1989; Lefebvre 1989), and epigenetic–syn-orogenic (e.g., Molak 1995; McGowan et

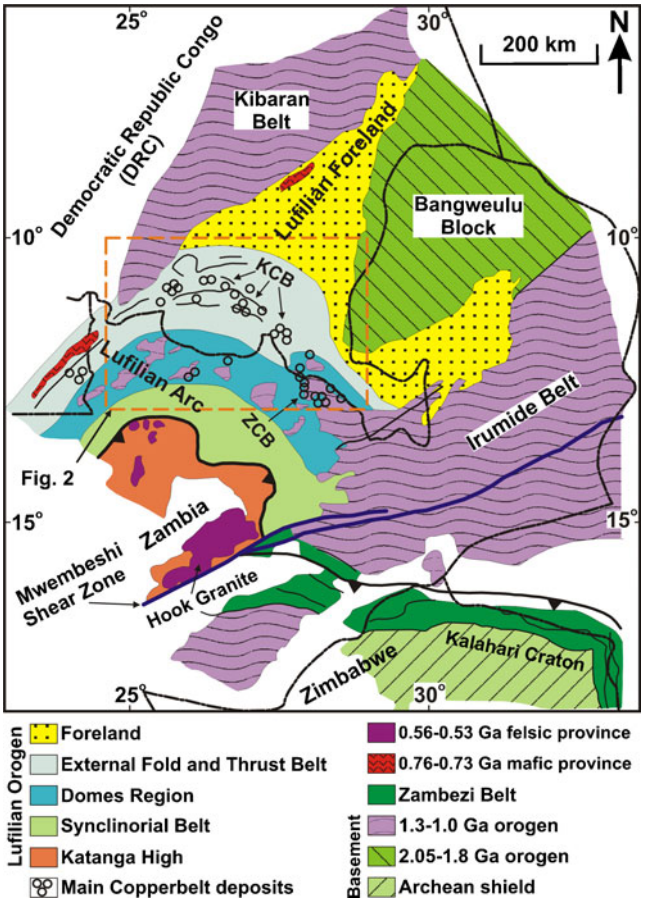

Fig. 1 Geologic map of the (Pan-African) Lufilian Orogen, showing the Lufilian Foreland, the tectonic zoning and structural architecture of the Lufilian Arc, and the distribution of the main deposits in the Katanga (*KCB*) and Zambian (*ZCB*) Copperbelts; modified from Porada (1989), Kampunzu and Cailteux (1999), and Selley et al. (2005)

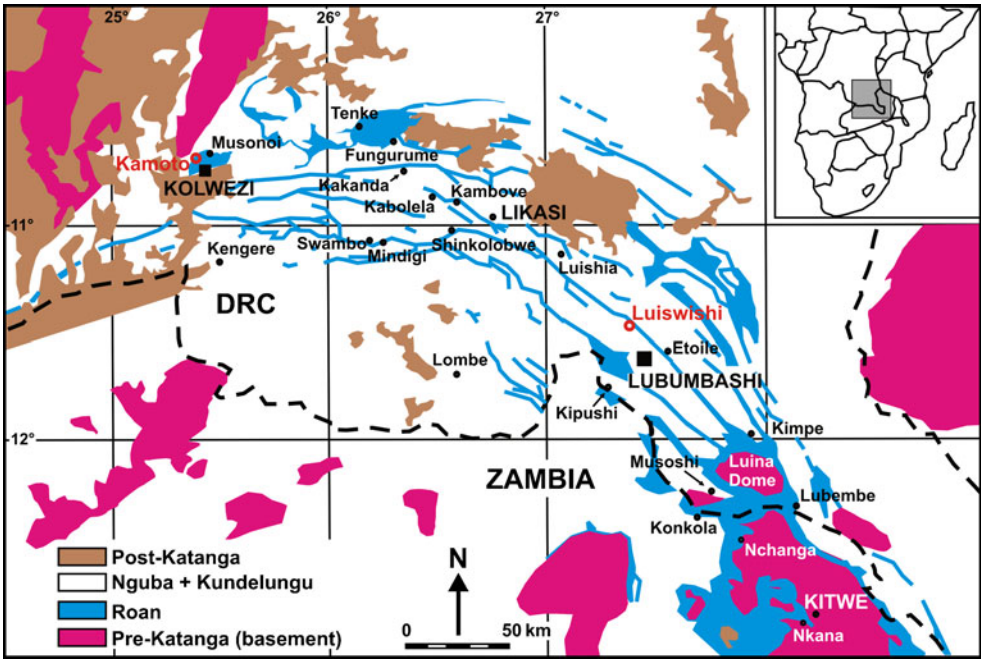

Fig. 2 Geologic map of the Central African Copperbelt with the location of the deposits at Kamoto and Luiswishi; modified from François (1974), Cailteux (1994), and Cailteux et al. (2005)

al. 2003, 2006) scenarios. However, the most recent research in both the Zambian (Selley et al. 2005; Hitzman et al. 2005; Brems et al. 2009) and Congolese (Cailteux et al. 2005; Dewaele et al. 2006; Muchez et al. 2007, 2008; El Desouky 2009) parts of the CACB suggest a multiphase origin for the ore deposits. El Desouky et al. (2007a, 2008b, 2009a) presented petrographic and microthermometric evidence for the presence of two main hypogene Cu–Co sulfide stages in the Katanga Copperbelt. The first mineralization stage is related to a fluid with a moderate temperature and salinity, whereas the second is related to a fluid with a significantly higher temperature and salinity (El Desouky et al. 2009a).

The aim of this paper is to shed light on the geology, petrography, and geochemistry of these two main sulfide ore stages. For this purpose, S, C, O, and Sr isotope analyses were performed on pyrite, Cu–Co sulfides, and associated carbonate minerals belonging to the two main stages. Sulfur isotope ratios were used to deduce the possible origin of sulfur in the ore sulfides, whereas C and O isotopes of the carbonates helped to evaluate the role of organic matter prior to and during mineralization as well as the possible temperatures and/or isotopic composition of the carbonate-precipitating fluids. Combined Sr and C–O isotope ratios were used to understand the behavior of the mineralizing/remobilizing fluids and the fluid-rock interaction regimes and to constrain the possible metal sources. These results were integrated with the fluid inclusion data of El Desouky et al. (2009a) in order to present a metallogenic model for each main mineralization stage. This results in a better understanding of the genesis of the sediment-hosted stratiform Cu–Co mineralization in the Katanga Copperbelt and most likely will enhance further exploration. For our study, two economic Cu–Co deposits were selected, i.e., Luiswishi and Kamoto. They occur respectively in the eastern and western parts of the Katanga Copperbelt (Fig. 2).

Regional geologic setting

The Neoproterozoic (Pan-African) Lufilian Orogen is composed of two main parts (Fig. 1): (1) the Lufilian Arc, a fold-and-thrust belt, which hosts the deposits of the CACB, and (2) the Lufilian Foreland (or the Kundelungu Plateau), a triangular-shaped area located to the NE of the Lufilian Arc. The Lufilian Foreland recently became an interesting ore district with the discovery of several stratiform (El Desouky et al. 2007b, 2008a, c) and vein-type (Haest et al. 2009) copper deposits. These deposits have a different genetic origin compared to the Cu–Co deposits of the CACB (El Desouky et al. 2008c; Kampunzu et al. 2009). The Lufilian Arc consists, from north to south, of four distinct tectonic zones (Fig. 1; Porada 1989; Kampunzu and Cailteux 1999): (1) the External Fold-and-Thrust Belt, (2) the Domes Region, (3) the Synclinorial Belt, and (4) the Katanga High. The deposits of the Katanga Copperbelt occur within the External Fold-and-Thrust Belt region, whereas most of the deposits of the Zambian Copperbelt are adjacent to the easternmost basement inlier of the Domes Region (Selley et al. 2005; Figs. 1 and 2).

The Cu–Co mineralization of the Katanga Copperbelt is hosted by the Mines Subgroup of the Katanga Supergroup (Fig. 3a). The Neoproterozoic Katanga Supergroup consists

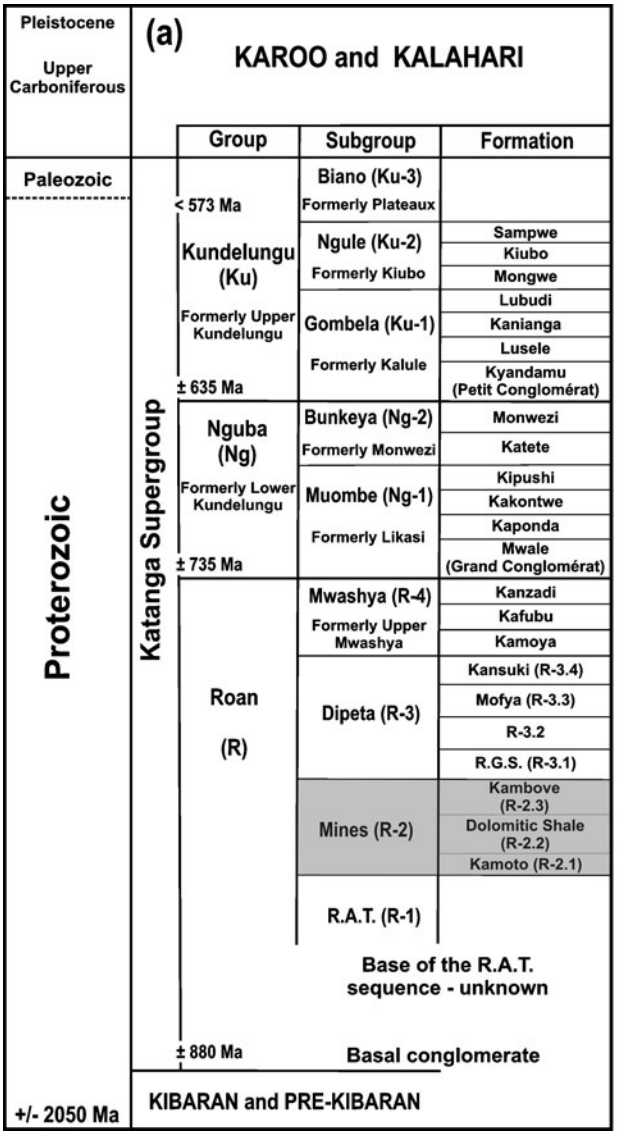

(b)

Formation	Member	Ore	Com. thick. (m)	Lo. thick. at Ls. (m)
Kambove (R-2.3) (Formerly C.M.N.) (up to 190m thick)	Upper Kambove (R-2.3.2) (Formerly Upper Calcaire à Minerai Noir or Upper C.M.N.)		40-100	not represented
	Lower Kambove (R-2.3.1) (Formerly Lower Calcaire à Minerai Noir or Lower C.M.N.)	Third Orebody (Lenses)	60-90	5.6-19.3
Dolomitic Shale (S.D.; R-2.2) (up to 140m thick)	S.D.-3b		30-125	13.1-31.7
	S.D.-3a			
	S.D.-2d			
	S.D.-2c			
	S.D.-2b			
	S.D.-2a			
	Black Ore Mineralized Zone (B.O.M.Z.; S.D.-1b)	Upper Orebody	5-15	1.7-7.4
	Shales Dolomitiques de Base (S.D.B.; S.D.-1a)			
Kamoto (R-2.1) (up to 50m thick)	Roches Siliceuses Cellulaires (R.S.C.)		0-30	1-4.3
	Roches Siliceuses Feuilletées (R.S.F.)	Lower Orebody	6-12.5	2.1-9
	Dolomites Stratifiées (D.Strat.)			
	Roches Argilo Talqueuses grises (gray R.A.T.)		0.5-5	3.9-8.1

Fig. 3 **a** General lithostratigraphic subdivision of the Katanga Supergroup in the Democratic Republic of Congo, compiled from Cailteux et al. (2005, 2007) and Batumike et al. (2007). **b** Detailed lithostratigraphic subdivision of the Mines Subgroup with the common thickness range of the units in the Katanga Copperbelt (*Com. thick.*) and corresponding local thicknesses at Luiswishi (*Lo. thick at Ls.*). The *figure* also highlights the location of the three typical stratiform Cu–Co orebodies (*Ore*) of the Katanga Copperbelt (compiled from Cailteux et al. 2003, 2005 and references therein)

of a ~5- to 10-km-thick sedimentary sequence that is commonly subdivided into three groups (Roan, Nguba, and Kundelungu), based on the regional occurrence of two correlative diamictites (Cailteux et al. 2005, 2007; Batumike et al. 2007; Fig. 3a). The lower diamictite is the "Grand Conglomérat" (Mwale Formation; Fig. 3a), which occurs at the base of the Nguba Group, and the upper diamictite is the "Petit Conglomérat" (Kyandamu Formation; Fig. 3a), situated at the base of the Kundelungu Group (Cailteux et al. 2005, 2007; Batumike et al. 2007; Fig. 3a). The oldest age for the bottom of the Roan Group is constrained by the 883±10-Ma U–Pb zircon age (Armstrong et al. 2005) for the Nchanga granite (Zambia; Fig. 1), which represents the youngest igneous activity that affected the underlying basement rocks prior to the sedimentation of the Roan rocks (Garlick and Brummer 1951). The age of the top of the Roan Group is constrained by the ~735-Ma altered volcanic pods, locally in contact with the glacial sediments of the Grand Conglomérat (Key et al. 2001). A maximum age for the deposition of the top of the Katanga Supergroup is constrained as 573±5 Ma (Master et al. 2005), the age of detrital muscovite grains from the Biano Subgroup at the top of the Kundelungu Group (Fig. 3a; Cailteux et al. 2007).

The Roan Group is subdivided into four subgroups (Fig. 3a), namely the Roches Argilo-Talqueuses (R.A.T.; R-1), Mines (R-2), Dipeta (R-3), and the Mwashya (R-4).

The R.A.T. Subgroup (R-1) is composed of dolomitic sandy-argillaceous oxidized sedimentary rocks. A change from oxidizing to reducing conditions defines the base of the Mines Subgroup (R-2), which is composed of alternating dolomite and dolomitic organic-rich shales/siltstones and which has been subdivided into three major units (Cailteux 1994; Cailteux et al. 2005; Fig. 3): the Kamoto (R-2.1), Dolomitic Shale (R-2.2), and Kambove (R-2.3) Formations. According to Cailteux (1994), the dolomites of the Mines Subgroup are related to platform-type carbonate deposition in intertidal, reef, and lagoonal environments, which maintained the reducing conditions. The Dipeta Subgroup (R-3) is characterized by sabkha-type sequences with oxidized sandy-argillaceous facies at the bottom and lagoonal-type carbonate facies at the top (François 1987; Cailteux 1994). The Kansuki Formation, at the top of the Dipeta Subgroup (Fig. 3a; Cailteux et al. 2007), is marked by rift-related mafic magmatic–volcanic rocks dated at 765 ±5 Ma (Key et al. 2001). The Mwashya Subgroup is characterized by an argillaceous–detrital succession of carbonaceous shales, siltstones, and sandstones with a basal sedimentary conglomeratic unit (Cailteux et al. 2007).

The Katanga sedimentary sequences were deformed during the Lufilian Orogeny, leading to the development of predominantly north-verging folds, thrusts, and nappes (Daly et al. 1984; Kampunzu and Cailteux 1999; Kampunzu et al. 2009). Based on the most recent geochronological data (Rainaud et al. 2005), the Lufilian Orogeny and its associated metamorphism span the period between ~592 and ~512 Ma and have a metamorphic peak at ~530 Ma (John et al. 2004). According to Lerouge et al. (2004) and Kampunzu et al. (2009), the age of ~592 Ma corresponds to the onset of the D2-Monwezian deformation phase of the Lufilian Orogeny. During the Lufilian Orogeny, felsic magmatism occurred along the Mwembeshi shear zone in Zambia forming the so-called Hook Granite massif (Fig. 1). This magmatic activity is constrained by a U–Pb zircon age of ~560–550 (Hanson et al. 1993). This age is considered as the most reliable age for the Lufilian Orogeny (Porada and Berhorst 2000).

Several lines of evidence have been provided for the former presence of evaporite layers in the R.A.T. and Dipeta Subgroups (Fig. 3a), i.e., below and above the Mines Subgroup (e.g., De Magnée and François 1988; Cailteux 1994; Cailteux and Kampunzu 1995; Jackson et al. 2003). These authors have stressed the importance of regional-scale salt tectonics in the deformation of the Katanga sedimentary sequences and the formation of the Katangan breccias. The most widely accepted model for the origin of the Katangan mega- and gigabreccias involves friction-related fragmentation along evaporitic horizons, which is associated with up to 150 km of syn-orogenic northward transport of thrust sheets during Lufilian inversion (François 1973; De Magnée and François 1988; Cailteux and Kampunzu 1995; Binda and Porada 1995; Kampunzu and Cailteux 1999; Porada and Berhorst 2000). According to Jackson et al. (2003), the origin of the Katangan gigabreccias (up to 10 km wide) is related to salt tectonics that began during basin extension and continued to basin inversion. In contrast with these tectonic hypotheses, Wendorff (2000, 2005) interpreted the Katangan megabreccias as syn-tectonic olistostrome/debris-flow conglomerate complexes.

According to Cailteux and Kampunzu (1995), the megabreccias are locally hundreds of meters to a kilometer across and contain rock types belonging to the Roan Group and in particular the Mines Subgroup (Fig. 4). They may form large elements of fragmented folds with folding preceding fragmentation and subsequent inclusion into the breccia body (e.g., at Luiswishi; Fig. 4). Included in these megabreccias, Cailteux and Kampunzu (1995) described the presence of three other breccia types of tectonic origin. Type 1 occurs between the megabreccia blocks (Fig. 4), i.e., the so-called heterogeneous intrusive breccias. Type 2 forms concordant centimeter- to meter-thick bodies under-

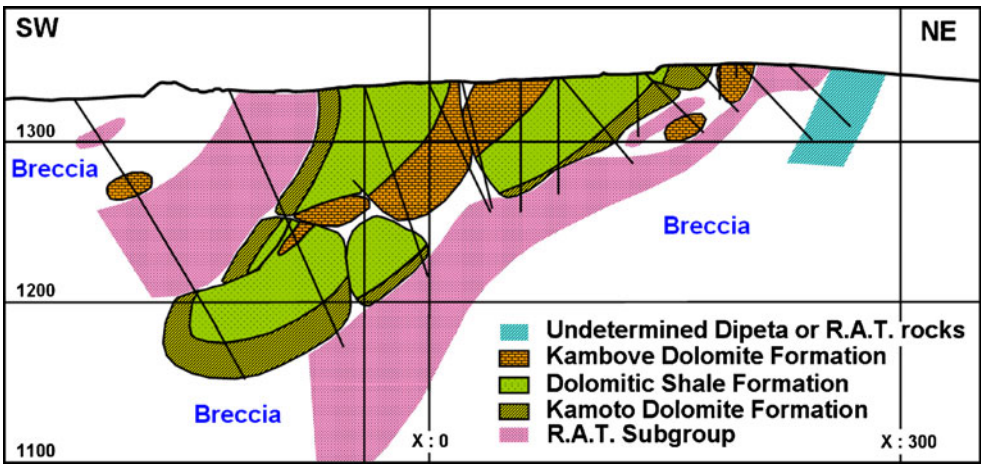

Fig. 4 Cross section showing the geology of the Luiswishi deposit and the tectonic megabreccia; modified from Cailteux et al. (2003, 2004)

lying the thrusted nappes or interbedded along the stratigraphical contact of the Mines Subgroup with both the R.A.T. and Dipeta Subgroups, i.e., the so-called heterogeneous concordant breccias. Type 3 occurs as discordant bodies along reverse faults in the folded structures (e.g., in the Mines Subgroup), i.e., the so-called monogeneous breccias. The breccias of type 1 and type 2 include angular to well-rounded, millimeter to several meter-size clasts mostly in an argillaceous–chloritic matrix, both derived from various sources (mostly Roan, but also Nguba and Kundelungu Groups), while type 3 contains angular fragments from the folded structures in a dolomite–quartz cement. Since these breccia types cut across the dismembered folded and thrusted Katanga sequences, they thus should have formed during and after the main folding/thrusting events of the Lufilian Orogeny (cf. Cailteux and Kampunzu 1995; Kampunzu and Cailteux 1999; Kampunzu et al. 2009).

Cu–Co mineralization

In the Katanga Copperbelt, the typical stratiform Cu–Co mineralization of the Mines Subgroup (Congo-type mineralization) is mainly concentrated in two stratigraphic positions, forming two main orebodies (Lower and Upper Orebody, respectively) hosted in the lower parts of the Kamoto and Dolomitic Shale Formations (Cailteux et al. 2005; Fig. 3b). The host rocks of the Lower Orebody consist of dolomitic siltstone, fine-grained dolomite, and silicified stromatolitic dolomite, alternating with chlorite-bearing dolomitic siltstone layers. The host rocks of the Upper Orebody include dolomitic shale and medium- to coarse-grained dolomite (Cailteux 1994; Cailteux et al. 2005). The two orebodies are separated by a generally barren/low-grade intermediate zone, i.e., the Roches Siliceuses Cellulaires Member (R.S.C.; Fig. 3b). This zone is composed of massive, reef-type stromatolitic dolomite. A third, subeconomic to economic orebody is hosted in the lower part of the Kambove Formation (Third Orebody; Fig. 3b). However, it is only developed locally at some places, e.g., at Luiswishi, Kambove-Ouest, and Luishia (Cailteux et al. 2005; Fig. 2). The host rocks of this orebody are part of a regressive sequence with rock types similar to the host rocks of the Lower and Upper Orebodies (Cailteux 1994; Cailteux et al. 2005). Other small subeconomic to economic occurrences are locally hosted by dark-gray to black organic-rich rocks of the S.D.2a, S.D.2d, and S.D.3b Members (Fig. 3b; Cailteux et al. 2005). Despite the high fragmented character of the Mines Subgroup, regional stratigraphic relations are remarkably uniform, with limited facies and thickness variation over the ~350-km strike length of the Katanga Copperbelt (Fig. 3b; Cailteux et al. 2005). The lateral variation of sulfides in the orebodies shows copper-rich zones grading into copper-poor zones and to pyritic barren zones, e.g., Kambove-Ouest (Cailteux 1994; Cailteux et al. 2005). The copper-poor and barren zones are called barren gaps, which are related to abrupt lateral paleoenvironmental lithofacies variations (Cailteux et al. 2005). According to Selley et al. (2005), the lateral lithofacies variations of the Zambian Copperbelt are consistently associated with structural and thickness perturbations, including syn-rift faults. Within the ore deposits, there is a remarkable lateral and vertical zoning of the copper-iron sulfides, which has been discussed in detail elsewhere (Cailteux et al. 2005, Selley et al. 2005, and references therein). In general, pyrite is often absent in the orebodies but occurs abundantly outside the mineralized zones and in the barren gaps, suggesting the replacement of pyrite in the rich-ore zones by Cu–Co sulfides (cf. Bartholomé et al. 1972).

The Luiswishi and Kamoto deposits are typical high-grade, Congo-type Cu–Co ore deposits (Cailteux et al. 2005; Muchez et al. 2008). The Luiswishi deposit occurs in a megabreccia located in the eastern part of the Katanga Copperbelt, ~26 km NW of Lubumbashi (Fig. 2). The Kamoto deposit occurs in the western part, in the megabreccia of Kolwezi, ~300 km NW of Lubumbashi (Fig. 2). The Luiswishi deposit is contained within a fractured, north-verging isoclinal synform with an axial plane dipping ~40° SW and has an areal footprint of ~1 km^2 (Cailteux et al. 2003, 2004; Fig. 4). The two limbs of the synform are composed of split blocks with rock types belonging to the Mines Subgroup in the central part and to those of the R.A.T. Subgroup in the external part (Fig. 4). The fold is cut by several faults parallel, oblique, and perpendicular to the fold axis (Cailteux et al. 2003, 2004; Fig. 4). At Luiswishi, all Cu–Co minerals in the weathered superficial zone and most of the minerals in the surface outcrops in the open pit mine (at the present stage) are oxidized, with malachite, chrysocolla, and azurite as the main supergene copper-bearing minerals, heterogenite as the main supergene cobalt mineral (ESM Fig. 1), and with hematite as the main by-product (Fig. 5). The supergene Cu–Co oxide minerals are mainly concentrated along bedding planes, in cavities, cracks (ESM Fig. 1a), and in fracture zones associated with faults (ESM Fig. 1b). In the boreholes, the abundance of supergene Cu–Co oxide minerals decreases with depth.

The Kamoto deposit forms part of the Kolwezi megabreccia klippe, an elliptical-shaped erosional remnant (~10 by 20 km) of what is thought to have been an extensive northward-directed thrust sheet emplaced in the northwestern part of the Katanga Copperbelt (François 1974). The klippe is composed of faulted blocks (with rock types belonging to the Roan Group) that form isoclinal synforms and antiforms (François 1973, 1974).

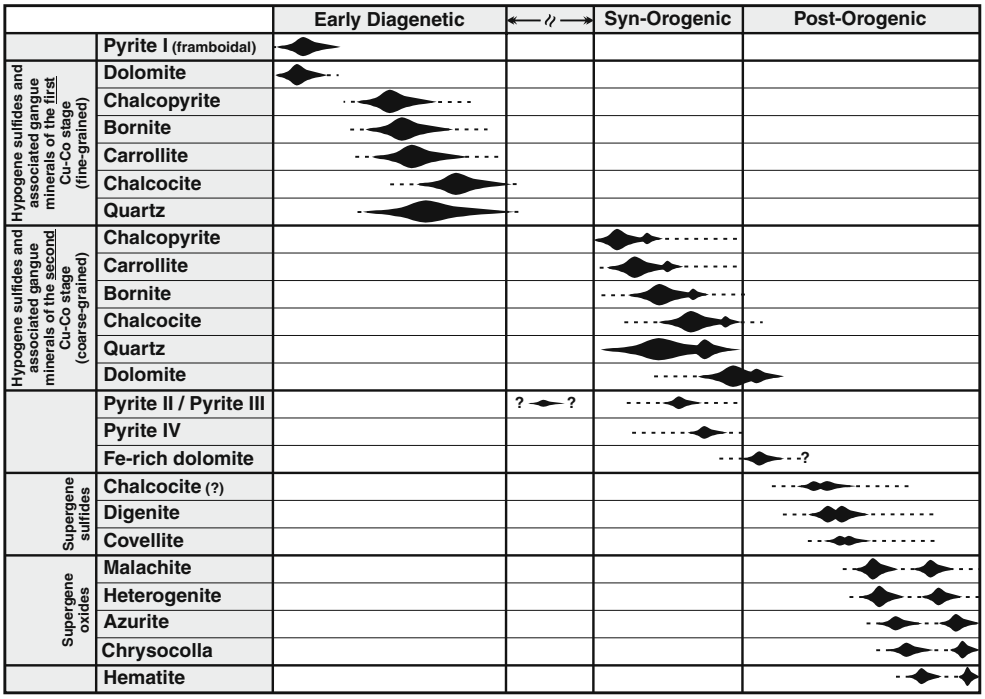

Fig. 5 Generalized paragenetic sequence for the Cu–Co mineralization at Luiswishi and Kamoto

Methodology

Sampling and sample characterization

A total of 239 fresh, unweathered core samples were collected from the different stratigraphic units of the Mines Subgroup: (1) 110 core samples were selected from three boreholes at Luiswishi (boreholes LSW1215, LSW1216, and LSW1301) and (2) 129 core samples were selected from Kamoto borehole F120, which is available in the archive collections of the University of Liège (Belgium). The Luiswishi samples were collected from all represented stratigraphic units of the Mines Subgroup (Fig. 3b). However, the samples from the Kamoto borehole F120 are only from the Kamoto and Dolomitic Shale Formations (Fig. 3b), as the Kambove Formation is not represented in the archive. Samples were polished, photographed, and stained with Alizarin Red S and potassium ferricyanide to distinguish between ferroan and nonferroan dolomite and calcite generations (Dickson 1966). Ninety-five thin sections and 60 polished sections were prepared from both deposits and carefully examined using both transmitted and reflected light microscopy. Additional four unweathered core samples were selected from two poorly mineralized/barren boreholes at Luiswishi (boreholes LSW1323 and LSW1324) for sulfur isotope analysis on pyrites. Furthermore, five unweathered barren host rock carbonate samples were selected from the outcrops of the Mines Subgroup at Kambove and the Dipeta Subgroup at Kabolela (DRC; Fig. 2) for Rb–Sr isotope analysis.

S, C, and O isotope analysis

The sulfur isotopic composition of the sulfides was determined, using standard polished sections, at the Scottish Universities Environmental Research Centre. Sixty-four in situ laser sulfur isotope analyses were performed on the different Cu–Co sulfide and pyrite generations from both Luiswishi and Kamoto. A spot area with a diameter of 300–400 μm was combusted using a SPECTRON LASERS 902Q CW Nd:YAG laser in the presence of excess oxygen (Fallick et al. 1992). In cases where the sulfide generation was not coarse enough, or fine-grained sulfides were not well aggregated to provide a single pure spot with such a diameter, several smaller pure spots were combined to obtain sufficient sulfur for isotope analysis. The released SO_2 gas was purified in a vacuum line operating similar to a conventional sulfur extraction line (cf. Kelley and Fallick 1990). The sulfur isotopic composition of the purified SO_2 gas was measured using a VG SIRA II gas mass spectrometer. Sulfur isotope compositions are reported in standard per mil relative to the Vienna Canyon Diablo Troilite (V-CDT). The analytical precision, based on replicate measurements of international standards NBS-123 and IAEA-S-3, as well as an internal lab standard CP-1 (SURRC), was ±0.2‰.

Oxygen and carbon isotope analyses were performed on 61 carbonate samples from Kamoto and 26 carbonate samples from Luiswishi. The samples were carefully selected from the different carbonate generations. The oxygen and carbon isotopic compositions were determined at the University of Erlangen (Germany). The carbonate

powders were reacted with 100% phosphoric acid (density >1.9; Wachter and Hayes 1985) at 75°C using a Kiel III online carbonate preparation line connected to a ThermoFinnigan 252 mass spectrometer. All values are reported in per mil relative to the Vienna Pee Dee Belemnite (V-PDB) by assigning a $\delta^{13}C$ value of +1.95 and a $\delta^{18}O$ value of −2.20 to NBS 19. Reproducibility was constrained by replicate analysis of laboratory standards and is better than ±0.04‰ (1σ) for both carbon and oxygen isotope ratios. The oxygen isotopic composition of dolomite was corrected using the fractionation factors given by Rosenbaum and Sheppard (1986).

Rb–Sr analysis

The Sr content and $^{87}Sr/^{86}Sr$ ratio were determined for a total of 33 samples from the different carbonate generations at Luiswishi and Kamoto and for the five barren host rock carbonate samples of Kambove and Kabolela. The Rb content and $^{87}Rb/^{86}Sr$ ratio were determined for 23 selected carbonate samples. The Rb–Sr analyses were performed at the Institute of Isotope Geochemistry and Mineral Resources (ETH Zurich, Switzerland). For this, ~30 mg of carbonate powders was weighed, spiked with a mixed ^{84}Sr–^{87}Rb tracer, and dissolved in 6 N HCl on a hot plate. After evaporation to dryness, the residues were redissolved in 3 N HNO_3. Rb and Sr were chemically separated with 3 N HNO_3 using EICHROM Sr resin on 50 µl Teflon columns, following the methods of Deniel and Pin (2001). The first HNO_3 wash (600 µl) containing the Rb fraction was evaporated to dryness, rewetted with 100 µl 6 N HCl, and dried again. Sr was stripped from the columns with 1 ml of H_2O. For mass spectrometry, Sr was loaded with a $TaCl_5$-HF-H_3PO_4 solution (Birck 1986) onto W single filaments. Rb was loaded with H_2O onto the evaporation ribbon of a Ta double-filament assemblage. All isotopic measurements were performed on a FINNIGAN MAT 262 solid-source mass spectrometer running in static multi-collection mode. Sr isotopic ratios were normalized to $^{86}Sr/^{88}Sr=0.1194$. Repeated static measurements of the NBS 987 standard over the duration of this study yielded an average $^{87}Sr/^{86}Sr$ ratio of 0.71024±3 (2σ mean, $n=16$). Total procedure blanks ($n=5$) amounted to 30 pg Sr and 4 pg Rb and were found to be negligible.

Results

Petrography and paragenesis

Macroscopic examination of stained hand specimens indicates that all the carbonate generations at both Luiswishi and Kamoto are dolomite and that the vast majority of the dolomite samples are Fe poor. Minor Fe-rich dolomite cement, with a blue staining color, was identified in some samples from both Luiswishi and Kamoto. The host rocks are characterized by two main lithotypes, i.e., dolomitic shale/siltstone and fine- to medium-grained dolomite. The color of the host rocks ranges from light gray to black, reflecting their high organic matter content (Cailteux 1994; Cailteux et al. 2005). Microscopically, the dolomitic host rocks are in places recrystallized to, or are overgrown with, coarse-grained dolomite, which may enclose crystals from the precursor fine-grained dolomite in its core.

Macroscopic examination of the samples allowed several Cu–Co sulfide mineralization styles to be distinguished: (1) disseminated Cu–Co sulfides, (2) Cu–Co sulfide lenses, with no associated gangue minerals that may range in thickness from 1 to several millimeters, (3) sulfides in nodules and layers (ESM Figs. 2b and 3a–i), (4) sulfides in veins (ESM Figs. 2b and 3f, j), and (5) sulfides in tectonic breccia cement (ESM Figs. 2a and 3k). The disseminated sulfides are fine- to coarse-grained and form individual grains or groups of grains, which run parallel to the stratification and are generally more abundant in the dolomite-rich beds than in the shaly ones. There is a consistent relationship between the size of the disseminated sulfides and the grain size of the host rock. The sulfides are often coarse-grained in the well-crystallized coarse-grained host rock dolomite and fine-grained in the medium- to fine-grained host rock dolomite and in the shaly horizons. In the nodules, layers, veins, and breccia cements, the Cu–Co sulfides are always associated with two main gangue minerals, quartz and dolomite, and the size of the sulfides is strongly related to the size of these gangue minerals regardless of the grain size of host rock.

Morphologically, two types of nodules and layers can be distinguished. Type I nodules are typically lenticular to oval, with their long axes parallel to the stratification, and are surrounded by locally ductile bend host rock laminae due to differential compaction at their borders (ESM Fig. 3a, b). In contrast, type II nodules display a greater variety in shape, e.g., circular or subrounded, and not necessarily parallel to the stratification (ESM Fig. 3c, d, g, i). Type I layers are thin, discontinuous (with respect to a hand specimen), or lenticular and have an irregular boundary with the host rock (ESM Fig. 3a, b), which is likely related to differential compaction at their borders. In contrast, type II layers are generally thicker, continuous, and have a sharp boundary with the host rock (ESM Fig. 3e, f, h, i). Although type II layers are parallel to stratification, in rare cases they cut and displace oblique veins (ESM Fig. 3f), indicating a late origin of these layers. In such cases, type II layers can be termed layer-parallel veins (e.g., Brems et al. 2009).

The veins, which cut both the stratification and type I nodules and layers, are millimeters to decimeters thick

(ESM Figs. 2b and 3f, j). They occur as straight individual veins or vein swarms with similar composition that branch and crosscut each other, suggesting the existence of several vein generations. The tectonic breccia cement encloses small, millimeter- to centimeter-size, fragments that are rounded to angular and have a dolomitic and/or shaly composition (ESM Figs. 2a and 3k). At Luiswishi, the breccia occurs in thick (up to 15 m of borehole intercept; ESM Fig. 2a) discordant bodies along faults cutting megabreccia blocks with folded strata belonging to the Mines Subgroup. This breccia corresponds to the "monogeneous breccia-type" of Cailteux and Kampunzu (1995), which formed during the Lufilian Orogeny. The Fe-rich dolomite generation overgrew and crosscut the nonferroan dolomite of the host rock, the two types of nodules and layers, the veins (ESM Fig. 3j), and the breccia cement. This indicates that the Fe-rich dolomite formed during a late stage of carbonate precipitation (Fig. 5).

Microscopically, type I nodules and layers are characterized by typically anhedral and fine-grained crystals of Cu–Co sulfides and gangue minerals (mainly dolomite and quartz; Figs. 6a–c and 7a–c). These nodules and layers

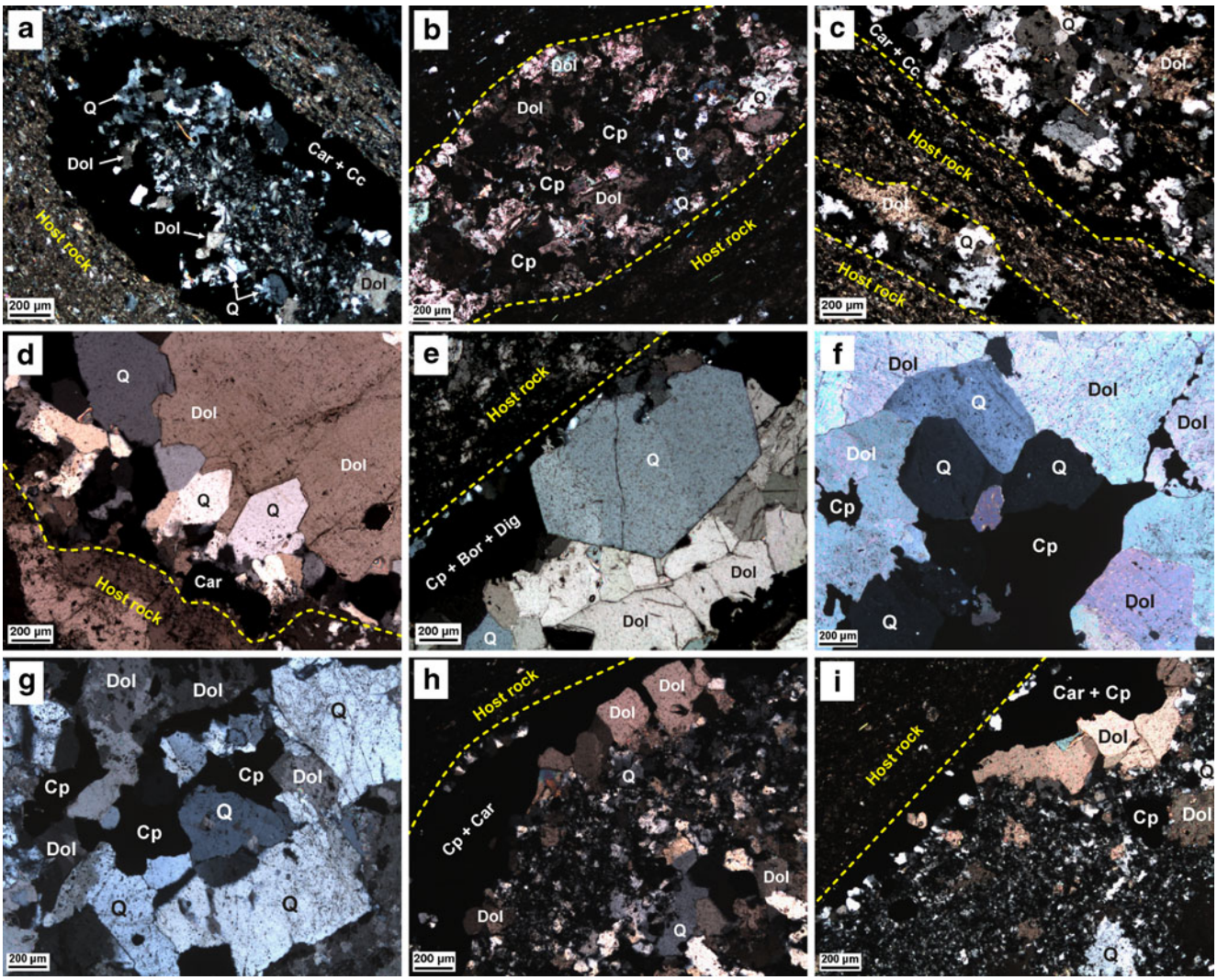

Fig. 6 Cross-polarized light photomicrographs of borehole samples from Kamoto and Luiswishi. **a**, **b** Type I nodules, from Kamoto (**a**) and Luiswishi (**b**), composed of mostly anhedral fine-grained dolomite (*Dol*) replaced by quartz (*Q*) and Cu–Co sulfides: carrollite (*Car*), chalcocite (*Cc*), and chalcopyrite (*Cp*). **c** Type I layers, from Kamoto, composed of dolomite replaced by carrollite, chalcocite, and quartz. **d** Part of a large type II nodule, from Luiswishi, hosted in medium-grained dolomite (B.O.M.Z. Member; Fig. 3a) and composed of subhedral to euhedral free-growing quartz and carrollite, both are overgrown and partly replaced with coarse-grained dolomite. **e** Part of a thick type II layer, from Luiswishi, composed of coarse-grained Cu sulfides (chalcopyrite and bornite "Bor" replaced by digenite "Dig") and quartz (euhedral free growing) overgrown and partly replaced with coarse-grained dolomite. **f**, **g** Coarse-grained quartz and chalcopyrite overgrown and partly replaced with coarse-grained dolomite in a vein (**f**) and breccia cement (**g**) from Luiswishi. **h**, **i** Recrystallized type I nodules (**h**) and layers (**i**), from Luiswishi, composed of a mixture of fine- to coarse-grained, anhedral to euhedral Cu–Co sulfides (chalcopyrite and carrollite), quartz, and dolomite

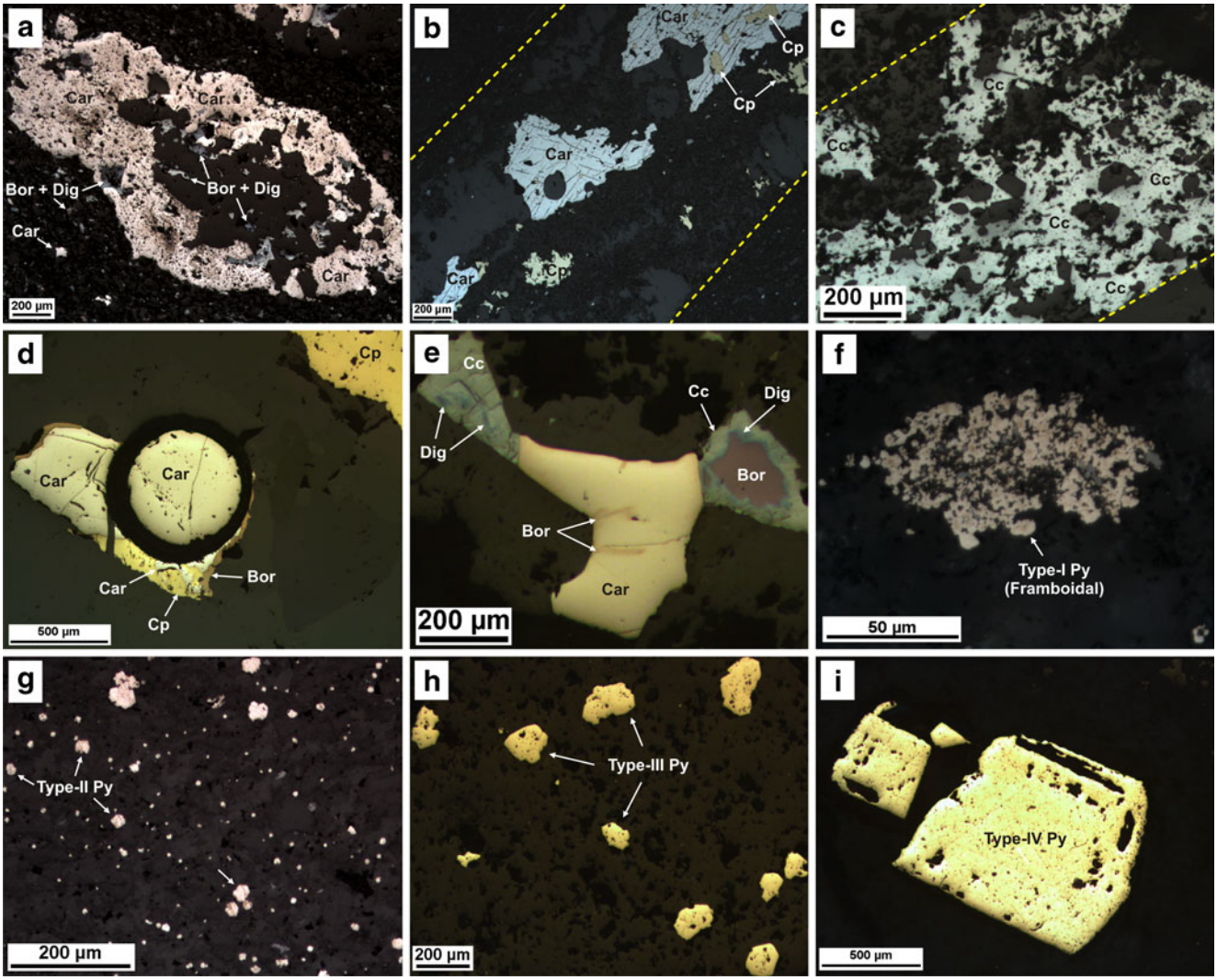

Fig. 7 Polarized reflected light photomicrographs from Luiswishi and Kamoto. **a** Type I nodule from Kamoto, with carrollite overgrown by minor bornite, and both are replaced by digenite. Fine-grained carrollite also occurs disseminated in the host rock. **b** Carrollite and chalcopyrite in the core of a type I layer from Luiswishi. **c** Fine-grained chalcocite in type I layer from Kamoto. **d** Coarse-grained carrollite and chalcopyrite in a vein from Luiswishi, both are overgrown by bornite. The *dark circle* highlights one of the spots combusted by in situ laser for sulfur isotope analysis on carrollite (sample LS06HA108-1; $\delta^{34}S_{carrollite}=19.4‰$; Table 1). **e** Carrollite replaced by bornite, which is replaced by chalcocite and digenite in a vein from Kamoto. **f** A cluster composed of very fine-grained anhedral framboidal pyrite (type I pyrite "Py") in a dark/organic-rich host rock from Luiswishi. **g** Disseminated fine-grained subhedral to euhedral pyrite crystals (type II pyrite; Luiswishi). **h** Disseminated medium-grained subhedral pyrite crystals (type III pyrite; Luiswishi). **i** Course- to very coarse-grained euhedral pyrite crystals (type IV pyrite; Luiswishi)

were interpreted as pseudomorphs after anhydrite and gypsum (Cailteux 1994; Muchez et al. 2008). In these nodules and layers, dolomite precipitated first and was subsequently replaced by Cu–Co sulfides and authigenic quartz (Figs. 5 and 6a–c; see also Muchez et al. 2008). In contrast, type II nodules and layers, the veins, and breccia cements are all composed of subhedral to euhedral coarse-grained free-growing Cu–Co sulfides, quartz, and dolomite (Figs. 6d–g and 7d, e). In these mineralization styles, quartz and Cu–Co sulfides precipitated first and are overgrown and replaced by dolomite (Figs. 5 and 6d–g). Type I nodules and layers are sometimes recrystallized and composed of a mixture of anhedral fine-grained to euhedral coarse-grained dolomite, Cu–Co sulfides, and quartz (Fig. 6h, i). The veins, breccia cement, type II, and recrystallized type I nodules and layers are often richer in Cu–Co sulfides compared to the nonrecrystallized type I nodules and layers (ESM Fig. 3). The occurrence of type I nodules and layers is often restricted to the three typical stratiform orebodies described above (Fig. 3b). In contrast, type II nodules and layers, the veins, and breccia cement occur at several stratigraphic levels in the Mines Subgroup and are more abundant at Luiswishi than at Kamoto. Although quartz and dolomite are the main gangue minerals

associated with all mineralization styles, the proportions of these minerals may vary significantly between different layers. It is also noticeable that quartz in veins is more abundant at Luiswishi than at Kamoto.

Both hypogene and supergene Cu–Co sulfides were observed at Luiswishi and Kamoto. The main hypogene Cu–Co sulfide minerals in all mineralization styles are chalcopyrite, carrollite, bornite, and chalcocite (Figs. 5 and 7a–e). Within a single mineralization style, chalcopyrite is always paragenetically the earliest (Figs. 5 and 7b, d) and chalcocite the latest (Figs. 5 and 7c, e). Locally, bornite is replaced by, or overgrew/replaced, carrollite (Figs. 5 and 7a, d, e). At Luiswishi, carrollite and chalcopyrite are most abundant (Fig. 7b, d) and are typically replaced by minor chalcocite (Fig. 5). Minor bornite occurs in the Lower Orebody only, especially in the gray R.A.T. Member (Fig. 7d). In the Lower and Upper Orebodies at Kamoto, the most abundant hypogene sulfides are carrollite and chalcocite (Fig. 7a, c) with rare relicts of earlier chalcopyrite. However, in the layers stratigraphically above the Upper Orebody (i.e., from S.D.-2a to S.D.-3b; Fig. 3b) at Kamoto, chalcopyrite is exceptionally abundant but only in type II nodules or minor breccia cements. At both Luiswishi and Kamoto, the hypogene sulfide minerals in the veins and breccia cement are often similar to the hypogene sulfide types in the surrounding type I nodules and layers and/or to the disseminated sulfides in the host rock. The main supergene sulfide minerals are digenite and covellite, both always replacing the earlier hypogene sulfides (Figs. 5 and 7a, e). The widespread occurrence of chalcocite at Kamoto could be related to supergene processes (Fig. 5; e.g., Selley et al. 2005).

Pyrite is an abundant mineral in the examined borehole samples (Fig. 7f–i). It occurs with varying amounts in the different units of the Mines Subgroup (Fig. 3b). Although minor disseminated pyrite occurs in the Third Orebody at Luiswishi, pyrite is almost absent in the mineralized stratigraphic units of the Lower and Upper Orebodies at both Luiswishi and Kamoto. Pyrite occurs in the stratigraphic units of the Lower and Upper Orebodies but only when these units are barren or poorly mineralized, e.g., in boreholes LSW1323 and LSW1324 at Luiswishi. Four different types of pyrite were recognized based on their grain size and crystal morphology. The first type (type I) represents typical disseminated framboidal pyrites, which are very fine-grained, anhedral, and characterized by an aggregated globular morphology (Fig. 7f). This pyrite type is paragenetically the earliest (Fig. 5) and often occurs in clusters associated with relicts of organic matter in the dark organic-rich host rocks. The second type (type II) is characterized by disseminated fine-grained subhedral to euhedral pyrite crystals, which typically occur abundantly and individually, i.e., not aggregated in clusters like the framboidal ones (Fig. 7g). The third type (type III) forms medium-grained subhedral to euhedral pyrite crystals that occur in clusters or disseminated (Fig. 7h). Types II and III occur associated with, or replace, type I pyrite. All pyrite types may be replaced or overgrown by Cu–Co sulfides (El Desouky 2009). The fourth and paragenetically latest pyrite type (type IV) is represented by disseminated euhedral coarse- to very coarse-grained crystals (Figs. 5 and 7i). This pyrite was only observed in barren breccia cements from the two poorly mineralized/barren boreholes of Luiswishi (boreholes LSW1323 and LSW1324). Bartholomé et al. (1971) reported similar pyrite types at Kamoto.

Sulfur isotopes

The results of in situ sulfur isotope analyses are shown in Table 1 and Fig. 8. The sulfur isotopic composition of Cu–Co sulfides from type I nodules and layers varies between −10.3‰ and +3.1‰ (n=27; Fig. 8b). The Cu–Co sulfides from type II nodules and layers, veins, and the breccia cement have $\delta^{34}S$ values which are mostly similar (−13.1‰ to +5.2‰; n=15) or significantly higher (+18.6‰ to +21.0‰; n=3) than the $\delta^{34}S$ values of the Cu–Co sulfides in type I nodules and layers (Fig. 8c). No significant difference exists between the $\delta^{34}S$ values of sulfides from type II nodules and layers, veins, and breccia cements (Table 1). The sulfur isotopic composition of the framboidal pyrites (i.e., type I) varies between −28.7‰ and +4.2‰ (n=9; Fig. 8a). In contrast, type IV pyrite has significantly higher $\delta^{34}S$ values (+14.2‰ to +15.1‰; n=3; Fig. 8d). Type II and type III pyrites are characterized by intermediate $\delta^{34}S$ values (+0.3‰ to +11.3‰; n=7), which overlap with the highest values of the $\delta^{34}S$ of framboidal pyrite grains and are lower than the $\delta^{34}S$ values of type IV pyrite (Fig. 8d).

Carbon and oxygen isotopes

Carbon and oxygen isotope analyses were performed on four different carbonate generations: (1) the massive dolomite (Fig. 6d) and the dolomitic shale/siltstone (Fig. 6a–c) of the host rocks, (2) the fine-grained dolomite associated with the Cu–Co sulfides in type I nodules and layers (Fig. 6a–c), (3) the coarse-grained free-growing dolomite associated with the Cu–Co sulfides in type II nodules and layers (Fig. 6d, e), veins (Fig. 6f), and breccia cement (Fig. 6g), and (4) the paragenetically late Fe-rich dolomite cement (ESM Fig. 3j). The results are shown in Table 2 and Fig. 9a for Kamoto and in Table 3 and Fig. 9b for Luiswishi. The host rock dolomites display a carbon isotopic composition that varies between $\delta^{13}C$=−7.8‰ and +1.3‰ (n=28) and an oxygen isotopic composition

Table 1 Sulfur isotopic composition of Cu–Co sulfides and pyrites form Luiswishi and Kamoto

Sample/spot	Style	Stratigraphy	Mineral	$\delta^{34}S$
Kamoto				
KA07HA10-1	N/L I	R.S.F.	Bor	0
KA07HA10-2	N/L I	R.S.F.	Bor	−3.1
KA07HA10-3	N/L I	R.S.F.	Cc	−1.8
KA07HA10-4	N/L I	R.S.F.	Cc	−1.4
KA07HA17-1	N/L I	S.D.B.	Car	−6
KA07HA17-2	N/L I	S.D.B.	Car	−8.1
KA07HA17-3	N/L I	S.D.B.	Car	−8.5
KA07HA17-4	N/L I	S.D.B.	Car	−10.3
KA07HA17-5	N/L I	S.D.B.	Car	−8.7
KA07HA18-1	N/L I	S.D.B.	Car	2.2
KA07HA18-2	N/L I	S.D.B.	Car	−3.1
KA07HA18-3	N/L I	S.D.B.	Car	−4.5
KA07HA18-4	N/L I	S.D.B.	Car	−3.8
KA07HA18-5	N/L I	S.D.B.	Car	3.1
KA07HA18-6	N/L I	S.D.B.	Car	−2.9
KA05VD052-1	N/L I	S.D.B.	Car	0.2
KA07HA21-1	N/L I	S.D.B.	Cc	−2.1
KA07HA21-2	N/L I	S.D.B.	Cc	−3.1
KA07HA21-3	N/L I	S.D.B.	Cc	−2.6
KA07HA21-4	N/L I	S.D.B.	Cc	−2.5
KA07HA35-4	Nodules II	S.D.-2d	Cpy	21
KA07HA03-1	Veins	D.Strat.	Car	−13.1
KA07HA05-1	Veins	D.Strat.	Bor	−5.8
KA07HA05-2	Veins	D.Strat.	Bor	−3.7
KA07HA12-1	Breccia	R.S.C.	Car	5.2
KA07HA12-2	Breccia	R.S.C.	Car	3.7
KA07HA15-1	Breccia	R.S.C.	Car	−4.3
KA07HA35-1	Type I Py.	S.D.-2d	Py	2.2
KA07HA35-2	Type I Py.	S.D.-2d	Py	4.2
KA07HA35-3	Type I Py.	S.D.-2d	Py	3.2
Luiswishi				
LS06HA080-1	N/L I	L. Kambove	Cpy	−6.8
LS06HA080-2	N/L I	L. Kambove	Cpy	−6.7
LS06HA024-1	N/L I	S.D.B.	Car	−9.0
LS06HA024-2	N/L I	S.D.B.	Car	−8.4
LS06HA107-1	N/L I	Gray R.A.T.	Bor	−0.9
LS06HA107-2	N/L I	Gray R.A.T.	Car	−2.2
LS06HA107-3	N/L I	Gray R.A.T.	Car	−1.0
LS06HA009-1	Nodules II	S.D.-3a	Cpy	−9.2
LS06HA009-2	Nodules II	S.D.-3a	Cpy	−11.4
LS06HA009-3	Nodules II	S.D.-3a	Cpy	−13.1
LS06HA023-1	Veins	B.O.M.Z.	Cpy	−1.8
LS06HA023-2	Veins	B.O.M.Z.	Cpy	−2.2
LS06HA023-3	Veins	B.O.M.Z.	Cpy	−2.1
LS06HA108-1	Veins	Gray R.A.T.	Car	19.4
LS06HA108-2	Veins	Gray R.A.T.	Cpy	18.6
LS06HA060-1	Breccia	L. Kambove	Cpy	−9.7
LS06HA060-2	Breccia	L. Kambove	Cpy	−9.4
LS06HA060-3	Breccia	L. Kambove	Cpy	−10.3
LS06HA080-3	Type I Py.	L. Kambove	Py	−8.9
LS06HA080-4	Type I Py.	L. Kambove	Py	−8.7
LS06HA080-5	Type I Py.	L. Kambove	Py	−8.9
LS06HA116-3	Type I Py.	R.S.C.	Py	−28.6
LS06HA116-4	Type I Py.	R.S.C.	Py	−28.7
LS06HA116-5	Type I Py.	R.S.C.	Py	−27.9
LS06HA111-1	Type II Py.	S.D.-2b+c	Py	6.7
LS06HA111-2	Type II Py.	S.D.-2b+c	Py	6.6
LS06HA116-1	Type III Py.	R.S.C.	Py	1
LS06HA116-2	Type III Py.	R.S.C.	Py	0.3
LS06HA126-1	Type III Py.	D.Strat.	Py	7.9
LS06HA126-2	Type III Py.	D.Strat.	Py	7.7
LS06HA126-3	Type III Py.	D.Strat.	Py	11.3
LS06HA119-1	Type IV Py.	R.S.C. breccia	Py	14.2
LS06HA119-2	Type IV Py.	R.S.C. Breccia	Py	14.4
LS06HA119-3	Type IV Py.	R.S.C. Breccia	Py	15.1

N/L I type I nodules and layers, *Nodules II* type II nodules, *Cpy* chalcopyrite, *Bor* bornite, *Car* carrollite, *Cc* chalcocite, *Py* pyrite

that ranges from $\delta^{18}O$=−14.5‰ to −7.2‰ (Fig. 9). The fine-grained dolomite in type I nodules and layers has a carbon isotopic composition that varies from $\delta^{13}C$=−9.9‰ to −1.4‰ (n=24) and an oxygen isotopic composition that ranges from $\delta^{18}O$=−14.1‰ to −7.7‰ (Fig. 9). The coarse-grained dolomites of type II nodules and layers, veins, and breccia cements display $\delta^{13}C$ values between −8.6‰ and +0.3‰ (n=27) and $\delta^{18}O$ values in the range of −24.0‰ to −10.3‰ (Fig. 9). No difference in the $\delta^{18}O$ and $\delta^{13}C$ values of dolomites from type II nodules and layers, veins, and breccia cements has been recognized (Tables 2 and 3). The $\delta^{13}C$ values of late Fe-rich dolomites range from −3.8‰ to −1.0‰ (n=8) and the $\delta^{18}O$ ranges from −24.0‰ to −16.8‰ (Fig. 9).

Rb–Sr results

The fine-grained dolomite of type I nodules and layers has $^{87}Sr/^{86}Sr$ values that vary from 0.70987 to 0.73576 (n=17; Table 4; Fig. 10a, b). The $^{87}Sr/^{86}Sr$ ratios of coarse-grained dolomite from type II nodules and layers, veins, and breccia cements varies between 0.70883 and 0.71215 (n=15; Table 4; Fig. 10a, b). The Sr isotopic composition of one poorly mineralized host rock dolomite sample from Kamoto is 0.70904 (Table 4; Fig. 10c). The

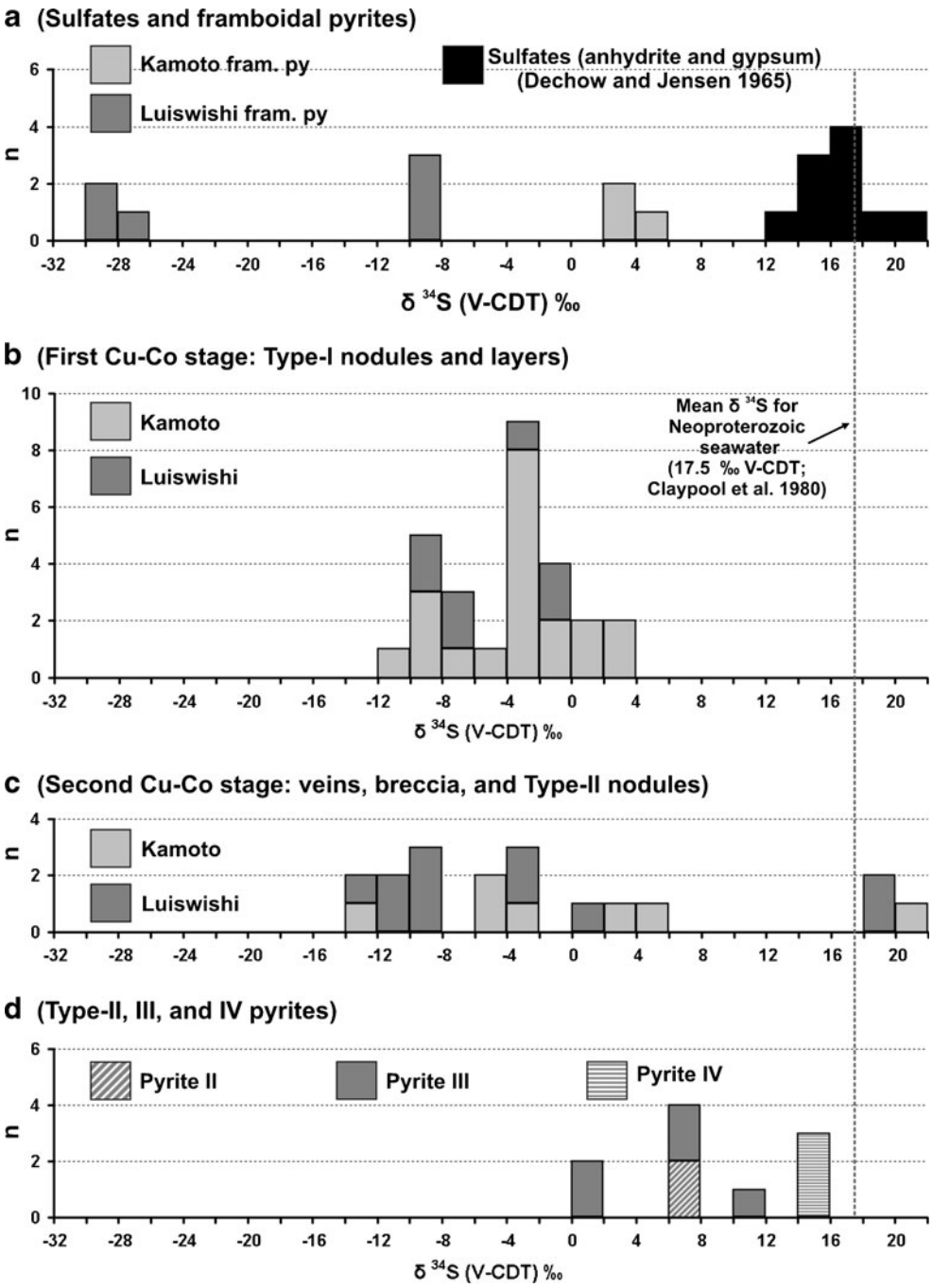

Fig. 8 Histograms showing the distribution of $\delta^{34}S$ values. **a** $\delta^{34}S$ of framboidal pyrite from Luiswishi and Kamoto and of sulfates from Dechow and Jensen (1965). **b** $\delta^{34}S$ of sulfides belonging to the first Cu–Co stage at Luiswishi and Kamoto. **c** $\delta^{34}S$ of sulfides belonging to the second Cu–Co stage at Luiswishi and Kamoto. **d** $\delta^{34}S$ of pyrite types II, III, and IV from Luiswishi

$^{87}Sr/^{86}Sr$ ratios of two barren host rock carbonate samples from the Mines Subgroup at Kambove are 0.70723 and 0.70754 (Table 4; Fig. 10c). The $^{87}Sr/^{86}Sr$ ratios of three barren host rock carbonate samples from the Dipeta Subgroup at Kabolela vary between 0.70774 and 0.70927 (Fig. 10c).

To determine the reason(s) for the variability of the $^{87}Sr/^{86}Sr$ ratios, e.g., in situ decay of ^{87}Rb and/or enrichment of Sr from an external radiogenic source, the Rb content and the $^{87}Rb/^{86}Sr$ ratio were determined for selected samples from each dolomite generation that have either low Sr concentrations or radiogenic $^{87}Sr/^{86}Sr$ ratios (Table 4). The striking observation is that the highest Rb contents (2.2 to 8.8 ppm) were obtained from the host rock dolomite samples with the least radiogenic Sr isotopic composition (Table 4). The Rb contents of all other dolomite samples are well below 1.5 ppm and even below 0.5 ppm (Table 4). The $^{87}Rb/^{86}Sr$ ratio for all samples varies from 0.0043 to 0.215 (Table 4), mostly too low to account for a significant in situ growth of radiogenic ^{87}Sr.

Table 2 C–O isotopic data for host rock dolomites and dolomites associated with Cu–Co mineralization at Kamoto

Sample	Style	Stratigraphy	$\delta^{18}O$	$\delta^{13}C$
KA05VD004	Host rock	Gray R.A.T.	−8.22	−3.62
KA05VD008	Host rock	D.Strat.	−7.18	−4.21
KA05VD009A	Host rock	D.Strat.	−7.18	−4.17
KA05VD009B	Host rock	D.Strat.	−7.15	−4.07
KA05VD010	Host rock	D.Strat.	−7.56	−4.32
KA05VD012	Host rock	D.Strat.	−10.54	−6.33
KA05VD013	Host rock	D.Strat.	−10.93	−7.05
KA05VD015	Host rock	D.Strat.	−10.32	−3.89
KA05VD016	Host rock	R.S.F.	−11.15	−4.69
KA05VD052	Host rock	S.D.B.	−14.48	−2.77
KA05VD064	Host rock	S.D.B.	−8.88	−4.90
KA05VD065A	Host rock	S.D.B.	−7.89	−2.45
KA05VD065B	Host rock	S.D.B.	−8.30	−2.69
KA05VD072	Host rock	B.O.M.Z.	−9.43	0.99
KA05VD075	Host rock	S.D.-2a+b+c	−9.34	0.10
KA05VD077	Host rock	S.D.-2a+b+c	−10.15	0.32
KA05VD079	Host rock	S.D.-2a+b+c	−9.06	1.08
KA05VD081	Host rock	S.D.-2a+b+c	−8.40	1.31
KA05VD089	Host rock	S.D.-2d	−9.70	−2.55
KA05VD090	Host rock	S.D.-3a	−9.41	−1.99
KA05VD011	N/L I	D.Strat.	−9.79	−7.02
KA05VD012	N/L I	D.Strat.	−10.21	−7.15
KA05VD014	N/L I	D.Strat.	−7.67	−5.23
KA07HA18	N/L I	S.D.B.	−12.23	−5.67
KA07HA20	N/L I	S.D.B.	−12.16	−3.13
KA07HA21	N/L I	S.D.B.	−12.37	−2.82
KA07HA22	N/L I	S.D.B.	−12.14	−3.00
KA07HA24	N/L I	S.D.B.	−10.18	−8.09
KA05VD026	N/L I	R.S.F.	−12.85	−3.86
KA07HA28	N/L I	S.D.B.	−10.95	−8.99
KA05VD052	N/L I	S.D.B.	−14.13	−3.32
KA05VD056	N/L I	S.D.B.	−11.33	−2.92
KA05VD062	N/L I	S.D.B.	−11.25	−7.10
KA05VD065A	N/L I	S.D.B.	−10.13	−9.93
KA05VD065B	N/L I	S.D.B.	−10.97	−9.64
KA05VD065C	N/L I	S.D.B.	−11.30	−9.64
KA05VD066A	N/L I	S.D.B.	−9.90	−9.77
KA05VD066B	N/L I	S.D.B.	−11.50	−9.77
KA07HA01	Nodules II	Gray R.A.T.	−24.01	−3.75
KA05VD052A	Nodules II	S.D.B.	−15.02	−4.47
KA05VD052B	Nodules II	S.D.B.	−15.18	−3.92
KA07HA05	Veins	D.Strat.	−13.66	−6.02
KA05VD013A	Veins	D.Strat.	−13.92	−5.86
KA05VD013B	Veins	D.Strat.	−13.42	−5.87
KA05VD052	Veins	S.D.B.	−12.12	−2.09
KA05VD064	Veins	S.D.B.	−11.14	−7.87
KA05VD067A	Veins	S.D.B.	−13.09	−3.20
KA05VD067B	Veins	S.D.B.	−12.05	−3.07
KA07HA15	Breccia	R.S.C.	−11.58	−5.23
KA05VD033	Breccia	R.S.C.	−10.33	−2.68
KA05VD034	Breccia	R.S.C.	−11.72	−2.91
KA05VD035	Breccia	R.S.C.	−11.15	−1.88
KA05VD040	Breccia	R.S.C.	−10.86	−4.85
KA05VD045	Breccia	R.S.C.	−10.74	−2.13
KA05VD002	Fe-rich dol.	R.A.T.	−23.98	−2.12
KA05VD005	Fe-rich dol.	Gray R.A.T.	−22.78	−3.16
KA05VD020	Fe-rich dol.	R.S.F.	−19.60	−3.10
KA05VD022	Fe-rich dol.	R.S.F.	−18.86	−2.60
KA05VD026	Fe-rich dol.	R.S.F.	−18.11	−1.07
KA05VD027A	Fe-rich dol.	R.S.F.	−17.57	−1.01
KA05VD027B	Fe-rich dol.	R.S.F.	−16.82	−1.00

N/L I type I nodules and layers, *Nodules II* type II nodules, *Fe-rich dol.* Fe-rich dolomite

Discussion

Cu–Co ore stages

The petrographic observations indicate the presence of two main generations of hypogene Cu–Co sulfides and associated gangue minerals (mainly quartz and dolomite) in the borehole samples of the Kamoto and Luiswishi deposits. The first generation is characterized by commonly fine-grained anhedral Cu–Co sulfides that occur disseminated in the mineralized host rocks (Fig. 7a) and frequently concentrated in type I nodules and layers (ESM Fig. 3a, b; Figs. 6a–c and 7a–c). The second generation is characterized by coarse-grained Cu–Co sulfides, which are also disseminated in the host rock but mostly occur in veins and tectonic breccia cements and in type II and recrystallized type I nodules and layers (ESM Fig. 3c–k; Figs. 6d–i and 7d, e). As the veins and breccia cements cut the stratification, including type I nodules and layers (ESM Figs. 2 and 3f, j, k), it is evident that the second generation is paragenetically later than the first one (Fig. 5).

According to El Desouky et al. (2009a), these two generations are the product of two main Cu–Co stages in the Katanga Copperbelt. The first is an early diagenetic typical stratiform stage, which is related to a hydrothermal fluid with a moderate temperature (115°C to ≤220°C) and salinity (11.3 to 20.9 wt.% NaCl equiv). The early diagenetic origin of this mineralization stage is supported by the differential compaction around type I nodules and layers, which indicates that they were formed, initially as anhydrite (cf. Muchez et al. 2008), before consolidation of the host rock (Müller 1967). This early diagenetic origin is

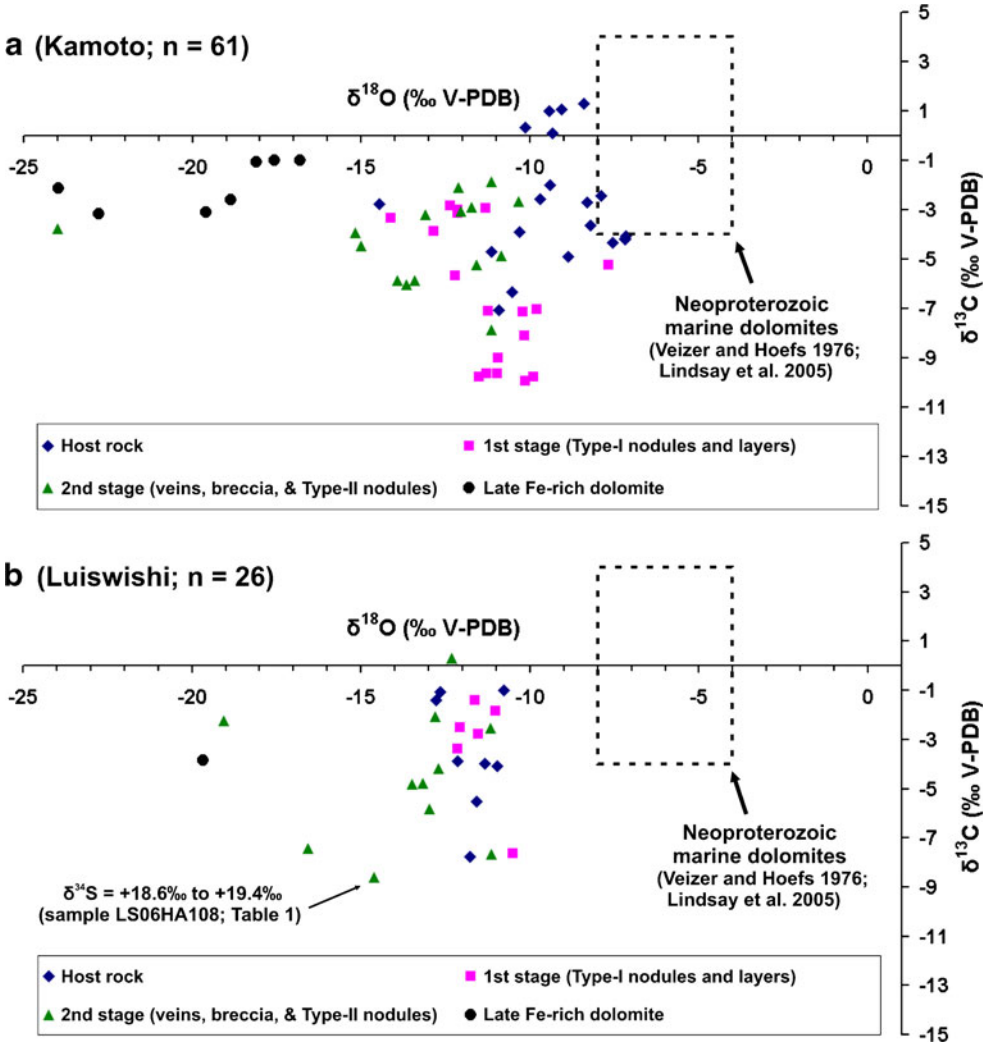

Fig. 9 Plots of $\delta^{13}C$ vs. $\delta^{18}O$ of host rock dolomite, of dolomite associated with sulfides belonging to the first (*1st*) and second (*2nd*) Cu–Co stages, and of late Fe-rich dolomite at Kamoto (**a**) and Luiswishi (**b**)

consistent with geochronological evidence for early diagenetic mineralization at the Konkola Mine in the Zambian Copperbelt (Fig. 2). Here, Selley et al. (2005) reported a six-point Re–Os isochron age of 816±62 Ma on chalcopyrite and bornite. The second main hypogene Cu–Co stage produced syn-orogenic stratiform to stratabound mineralization, which is related to a hydrothermal fluid with high temperature (270°C to 385°C) and salinity (35 to 45.5 wt.% NaCl equiv). The association of the coarse-grained Cu–Co sulfides of this stage to tectonic breccia cements that formed during the Lufilian Orogeny (Cailteux and Kampunzu 1995; Kampunzu and Cailteux 1999) supports this syn-orogenic origin. The crosscutting veins observed at both Luiswishi and Kamoto indicate that the sulfides of the second stage could have formed in several periods during the wide range (~592–512 Ma; Rainaud et al. 2005) of the Lufilian Orogeny (e.g., Brems et al. 2009). This multistage syn-orogenic origin for the second Cu–Co stage is supported by ore geochronological data from the entire CACB. A review of this data (see Selley et al. 2005; El Desouky et al. 2009a) indicates that the syn-orogenic ores were possibly formed during three main stages that overlap with the initial (~592 Ma), peak (~530 Ma), and post peak (~512–500 Ma) ages of the Lufilian Orogeny (John et al. 2004; Rainaud et al. 2005).

Our observations indicate that the hypogene sulfide minerals in the veins and breccia cements of the second generation are often similar to the hypogene sulfide types in the surrounding type I nodules and layers and/or the disseminated sulfides in the host rock. This similarity could suggest sulfide remobilization from the first Cu–Co stage during the second one. The remobilization of early sulfides into late crosscutting veins has been documented at several locations in the CACB (cf. Mendelsohn 1961a, b; Garlick 1965; Cailteux et al. 2005; Selley et al. 2005).

In addition to the two main hypogene Cu–Co stages defined above, one or several Cu–Co supergene sulfide and oxide stages occurred in the Katanga Copperbelt (Fig. 5). The occurrence of supergene Cu–Co oxide minerals, e.g., malachite and heterogenite, concentrated along cracks and faults in the Luiswishi mine (ESM Fig. 1) indicates that the Cu and Co metals of the hypogene ore minerals were

Table 3 C–O isotopic data for host rock dolomites and dolomites associated with Cu–Co mineralization at Luiswishi

Sample	Style	Stratigraphy	$\delta^{18}O$	$\delta^{13}C$
LS06HA003	Host rock	L. Kambove	−10.78	−0.99
LS06HA045	Host rock	B.O.M.Z.	−12.15	−3.86
LS06HA068	Host rock	B.O.M.Z.	−11.35	−3.98
LS06HA070	Host rock	S.D.B.	−11.59	−5.53
LS06HA083	Host rock	S.D.-3a	−12.66	−1.07
LS06HA098	Host rock	S.D.B.	−10.96	−4.09
LS06HA095	Host rock	B.O.M.Z.	−12.78	−1.40
LS06HA105	Host rock	D.Strat.	−11.78	−7.76
LS06HA004	N/L I	L. Kambove	−11.64	−1.41
LS06HA005	N/L I	L. Kambove	−11.54	−2.77
LS06HA034	N/L I	D.Strat.	−10.51	−7.64
LS06HA057	N/L I	L. Kambove	−12.06	−2.49
LS06HA078	N/L I	L. Kambove	−11.03	−1.83
LS06HA080	N/L I	L. Kambove	−12.15	−3.36
LS06HA009	Nodules II	S.D.-3a	−12.32	0.30
LS06HA043	Nodules II	B.O.M.Z.	−11.15	−7.65
LS06HA067	Nodules II	B.O.M.Z.	−11.18	−2.52
LS06HA016	Veins	S.D.-2d	−13.49	−4.81
LS06HA025	Veins	R.S.C.	−16.57	−7.41
LS06HA052	Veins	S.D.-3a	−13.18	−4.78
LS06HA057	Veins	L. Kambove	−12.72	−4.17
LS06HA108	Veins	Gray R.A.T.	−14.61	−8.61
LS06HA060	Breccia	L. Kambove	−12.81	−2.07
LS06HA061	Breccia	L. Kambove	−12.98	−5.83
LS06HA064	Breccia	S.D.-2a	−19.07	−2.25
LS06HA062	Fe-rich dol.	S.D.-2b+c	−19.68	−3.83

N/L I type I nodules and layers, *Nodules II* type II nodules, *Fe-rich dol.* Fe-rich dolomite

leached, remobilized, and enriched by surface/near-surface processes, during the exposure of the host rocks (Schwartz 1934; Chávez 2000). The supergene enrichment could cause a major increase in the Cu–Co ore grade, from a few percent up to 25%, and is therefore of great economic importance (Dewaele et al. 2006 and references therein). The association of supergene minerals to faults and cracks also highlights the role of the tectonic structures in remobilizing and upgrading the hypogene mineralization, which is in agreement with the remote sensing observations of Dewaele et al. (2006). These authors suggested a close relationship between major structural lineaments (e.g., faults) and Cu–Co mineralization in the Katanga Copperbelt. They proposed that faults most likely played a significant role for the migration of at least the supergene enrichment fluids. In addition to this structurally controlled supergene enrichment, De Putter et al. (2008) provided REE patterns that linked the presence of supergene Cu–Co enrichment (e.g., malachite and heterogenite) to major carbonate karstification event(s), which affected the Lufilian Arc possibly during the Carboniferous–Triassic, the Oligocene–Miocene, and/or most likely during the Cretaceous (De Putter et al. 2008).

Origin of sulfur

Taking into account the sedimentary environment, the abundant presence of former evaporite nodules and layers in the host rock (cf. Muchez et al. 2008 and references therein), the presence of evaporite layers below and above the mineralized rocks (Cailteux 1994; Cailteux and Kampunzu 1995; Jackson et al. 2003), and the absence of a widespread magmatic sulfur source (cf. Selley et al. 2005), it is concluded that the Cu–Co sulfides of the Katanga Copperbelt obtained their sulfur by either bacterial or thermochemical reduction of sedimentary sulfate. A mean $\delta^{34}S$ value of +17.5‰±3‰ is suggested for Neoproterozoic seawater at the time of deposition of the Roan Group (Holser and Kaplan 1966; Holser 1977; Claypool et al. 1980; Hurtgen et al. 2002; Fig. 8). This value is supported by $\delta^{34}S$ analyses on anhydrite from the Roan Group, which mostly plot in the range between 14‰ and 19‰ (Fig. 8a), with some $\delta^{34}S$ values reaching +25.6‰ (Dechow and Jensen 1965; Claypool et al. 1980; Annels 1989; Selley et al. 2005). However, it cannot be excluded that also late diagenetic anhydrites have been analyzed (cf. Brems et al. 2009).

Framboidal pyrite is the most common typical by-product of bacterial sulfate reduction (BSR), a process that occurs at temperatures from 0°C up to about 60–80°C (Machel and Foght 2000; Machel 2001). The sulfur isotopic composition of the Kamoto and Luiswishi framboidal pyrite (type I pyrite; $\delta^{34}S$=−28.7 to +4.2; Table 1; Fig. 8a) is depleted by 13.3‰ to 46.2‰ compared to the mean $\delta^{34}S$ of Neoproterozoic seawater. This large range of fractionation is indeed consistent with fractionations for bacterial sulfate reduction (15‰ to 60‰; Ohmoto 1986; Machel et al. 1995). Similar light $\delta^{34}S$ values (−17‰ to −1‰) were reported by McGowan et al. (2003, 2006) for early diagenetic black shale-hosted pyrite from the Lower Orebody at Nchanga (Zambia; Fig. 2). The authors related this $\delta^{34}S$ signature to bacterial sulfate reduction of seawater sulfate.

There are two possible sulfur sources for the sulfides in the type I nodules and layers (first Cu–Co stage): (1) BSR of anhydrite that was present in these nodules and/or (2) thermochemical sulfate reduction (TSR) of the anhydrite at mean temperatures of 160°C to 180°C (El Desouky et al. 2009a; Dewaele et al. 2006). At 160–180°C, an open-system TSR should result in $\Delta^{34}S_{SO4\text{-}sulfides}$ of about 12‰ to 14‰ (Harrison and Thode 1957; Kiyosu and Krouse 1990; Machel et al. 1995), and the by-product carbonate

Table 4 Rb–Sr isotopic and concentration data for dolomites associated with Cu–Co mineralization at Luiswishi and Kamoto and for barren/poorly mineralized host rock carbonates from Kamoto, Kambove, and Kabolela

Sample	Style	Stratigraphy	$^{87}Rb/^{86}Sr$	2σ	$^{87}Sr/^{86}Sr$	2σ	Rb (ppm)	2σ	Sr (ppm)	2σ	$(^{87}Sr/^{86}Sr)i$ (816Ma)	$(^{87}Sr/^{86}Sr)i$ (590Ma)
Kamoto												
KA07HA04	N/L I	D.Strat.	0.0177	0.0003	0.71021	0.00002	0.0437	0.0005	7.13	0.05	0.71000	n.r.
KA05VD011	N/L I	D.Strat.	n.d.	n.d.	0.71025	0.00002	n.d.	n.d.	31.18	0.22	n.d.	n.d.
KA05VD012	N/L I	D.Strat.	0.0043	0.0001	0.71120	0.00018	0.0240	0.0003	16.11	0.11	0.71115	n.r.
KA07HA18	N/L I	S.D.B.	n.d.	n.d.	0.71309	0.00002	n.d.	n.d.	19.76	0.11	n.d.	n.d.
KA07HA20	N/L I	S.D.B.	0.0130	0.0002	0.73408	0.00002	0.0832	0.0009	18.51	0.08	0.73393	n.r.
KA07HA21	N/L I	S.D.B.	0.0933	0.0010	0.73576	0.00002	0.7182	0.0073	22.33	0.10	0.73467	n.r.
KA07HA22	N/L I	S.D.B.	0.0260	0.0004	0.71493	0.00001	0.1324	0.0015	14.75	0.12	0.71463	n.r.
KA07HA24	N/L I	S.D.B.	0.0561	0.0006	0.71038	0.00003	0.8110	0.0077	41.87	0.32	0.70973	n.r.
KA07HA28	N/L I	S.D.B.	0.0928	0.0008	0.71332	0.00002	1.0640	0.0091	33.18	0.16	0.71224	n.r.
KA05VD062	N/L I	S.D.B.	n.d.	n.d.	0.71024	0.00002	n.d.	n.d.	29.32	0.23	n.d.	n.d.
KA05VD065	N/L I	S.D.B.	n.d.	n.d.	0.71223	0.00003	n.d.	n.d.	40.61	0.26	n.d.	n.d.
KA05VD066	N/L I	S.D.B.	n.d.	n.d.	0.71012	0.00001	n.d.	n.d.	41.08	0.22	n.d.	n.d.
KA07HA01	Nodules II	Gray R.A.T.	n.d.	n.d.	0.70919	0.00001	n.d.	n.d.	42.29	0.46	n.d.	n.d.
KA05VD052	Veins	S.D.B.	0.049	0.001	0.70952	0.00002	0.4430	0.0090	25.96	0.28	n.r.	0.70910
KA05VD067	Veins	S.D.B.	0.030	0.001	0.70933	0.00001	0.3546	0.0071	33.66	0.37	n.r.	0.70907
KA07HA05	Veins	D.Strat.	n.d.	n.d.	0.70926	0.00002	n.d.	n.d.	40.18	0.44	n.d.	n.d.
KA07HA15	Breccia	R.S.C.	0.011	0.0003	0.70883	0.00002	0.0229	0.0005	5.85	0.06	n.r.	0.70873
KA05VD081	Host rock	S.D.-2a+b+c	0.0484	0.0013	0.70904	0.00001	0.572	0.012	34.21	0.45	n.r.	0.70863
Luiswishi												
LS06HA107	N/L I	Gray R.A.T.	n.d.	n.d.	0.70987	0.00001	n.d.	n.d.	30.21	0.33	n.d.	n.d.
LS06HA034	N/L I	D.Strat.	n.d.	n.d.	0.71090	0.00002	n.d.	n.d.	11.36	0.12	n.d.	n.d.
LS06HA005	N/L I	L. Kambove	0.046	0.001	0.71104	0.00002	0.5242	0.0104	33.11	0.36	0.71051	n.r.
LS06HA067	N/L I	B.O.M.Z.	0.130	0.003	0.71046	0.00001	0.1086	0.0022	2.42	0.03	0.70895	n.r.
LS06HA080	N/L I	L. Kambove	n.d.	n.d.	0.71022	0.00003	n.d.	n.d.	22.46	0.24	n.d.	n.d.
LS06HA009	Nodules II	S.D.-3a	n.d.	n.d.	0.71119	0.00001	n.d.	n.d.	64.55	0.71	n.d.	n.d.
LS06HA043	Nodules II	B.O.M.Z.	0.115	0.003	0.71032	0.00001	0.3980	0.0079	10.04	0.11	n.r.	0.70935
LS06HA040	Nodules II	R.S.C.	n.d.	n.d.	0.71046	0.00004	n.d.	n.d.	21.12	0.23	n.d.	n.d.
LS06HA016	Veins	S.D.-2d	n.d.	n.d.	0.71013	0.00002	n.d.	n.d.	30.21	0.33	n.d.	n.d.
LS06HA023	Veins	B.O.M.Z.	0.111	0.003	0.71137	0.00002	0.5765	0.0115	14.98	0.16	n.r.	0.71043
LS06HA108	Veins	Gray R.A.T.	n.d.	n.d.	0.71002	0.00001	n.d.	n.d.	24.11	0.26	n.d.	n.d.
LS06HA070	Veins	S.D.B.	0.070	0.002	0.71094	0.00001	0.4822	0.0096	19.85	0.22	n.r.	0.71035
LS06HA060	Breccia	L. Kambove	n.d.	n.d.	0.71004	0.00002	n.d.	n.d.	47.14	0.51	n.d.	n.d.
LS06HA064	Breccia	S.D.-2a	n.d.	n.d.	0.71001	0.00002	n.d.	n.d.	61.7	0.67	n.d.	n.d.
LS06HA037	Breccia	R.S.F.	0.215	0.005	0.71215	0.00002	1.4929	0.0298	20.11	0.22	n.r.	0.71034
Kabolela												
KB08HA2	Host rock	Dipeta	0.0578	0.0015	0.70796	0.00002	2.172	0.046	108.75	1.43	n.r.	0.70748

Table 4 (continued)

Sample	Style	Stratigraphy	$^{87}Rb/^{86}Sr$	2σ	$^{87}Sr/^{86}Sr$	2σ	Rb (ppm)	2σ	Sr (ppm)	2σ	$(^{87}Sr/^{86}Sr)i$ (816Ma)	$(^{87}Sr/^{86}Sr)i$ (590Ma)
KB08HA3	Host rock	Dipeta	0.0254	0.0007	0.70927	0.00002	0.776	0.016	88.43	1.16	n.r.	0.70906
KB08HA6	Host rock	Dipeta	0.1000	0.0027	0.70774	0.00002	8.828	0.187	255.49	3.54	n.r.	0.70690
Kambove												
KM08HA1	Host rock	Mines	0.0371	0.0010	0.70723	0.00001	3.271	0.069	255.38	3.37	n.r.	0.70692
KM08HA2	Host rock	Mines	0.0512	0.0013	0.70754	0.00001	5.738	0.121	324.01	4.27	n.r.	0.70710
Basement (Ngoyi et al. 1991)												
Luina 1	Granitic	Basement	3.817	NA	0.778	NA	211	NA	161	NA	0.73351	0.74589
Luina 5	Granitic	Basement	7.751	NA	0.846	NA	256	NA	96.7	NA	0.75567	0.78079
Luina M5	Granitic	Basement	3.879	NA	0.777	NA	212	NA	160	NA	0.73179	0.74437
Luina ST1	Granitic	Basement	3.302	NA	0.778	NA	263	NA	232	NA	0.73952	0.75022
Lubembe 1	Granitic	Basement	1.218	NA	0.733	NA	154	NA	367	NA	0.71880	0.72275
Lubembe 9	Granitic	Basement	2.462	NA	0.743	NA	175	NA	206	NA	0.71431	0.72229
Lubembe 12	Granitic	Basement	1.719	NA	0.735	NA	125	NA	210	NA	0.71497	0.72054

Whole-rock Rb–Sr isotopic and concentration data for seven samples from the granitic basement at Luina (after Ngoyi et al. 1991) are also listed for comparison

n.d. not determined, *n.r.* not relevant, $(^{87}Sr/^{86}Sr)i$ initial $^{87}Sr/^{86}Sr$ ratio recalculated to the given age (816 or 590 Ma), *N/L I* type I nodules and layers, *Nodules II* type II nodules

normally should have a coarse-grained texture (cf. Machel 1987a, 2001). This fractionation becomes much lower if the system is partially or completely closed (Ohmoto 1986; Machel et al. 1995; Hoy and Ohmoto 1989). The Cu–Co sulfides of the first Cu–Co stage have $\delta^{34}S$ values in the range of −10.3‰ to +3.1‰ (Table 1), which indicate a $\Delta^{34}S_{SO4\text{-}sulfides}$ in the range of 14.4‰ to 27.8‰ relative to the mean $\delta^{34}S$ of Neoproterozoic seawater (Fig. 8a, b). As the sulfides of the first Cu–Co stage have $\delta^{34}S$ values similar to the $\delta^{34}S$ values of framboidal pyrite (Fig. 8a, b), have a large fractionation that is not consistent with even open-system TSR at 160–180°C, and because the dolomite in the type I nodules and layers is fine-grained, it is concluded that the sulfides of the first Cu–Co stage obtained their sulfur from BSR (El Desouky et al. 2009b) and that this fine-grained dolomite is a by-product of the BSR process (see also Muchez et al. 2008). The variability in the $\delta^{34}S$ values of framboidal pyrite and of the sulfides of the first Cu–Co stage in the same sample (up to 4.3‰ in sample KA07HA17; Table 1), from one sample to another (up to 19‰ between samples LS06HA080 and LS06HA116; Table 1) or from Luiswishi to Kamoto (Fig. 8a, b), could be related to the $\delta^{34}S$ variability in the parent sulfate source combined with a variability in temperature, sulfate concentration, organic substrate, type of reducing bacteria populations during BSR, and/or heterogeneous bacterial colonization (cf. Ohmoto 1986; Hoy and Ohmoto 1989; Machel et al. 1995; Kohn et al. 1998; Canfield 2001; Hurtgen et al. 2005).

H_2S, which is a main and abundant by-product of BSR (Machel 1987b, 2001; Machel et al. 1995), most likely reacted with Cu–Co metals from a hydrothermal mineralizing fluid to form Cu–Co sulfides in the mineralized horizons (cf. Muchez et al. 2008). Muchez et al. (2008) explained that the release of hydrogen ions during sulfide precipitation caused a decrease in pH and thus precipitation of the authigenic quartz, which often occurs in type I nodules and layers. This precipitation model for the Cu–Co sulfides in type I nodules and layers (Muchez et al. 2008) confirms our earlier suggestion for an early diagenetic origin for the first Cu–Co mineralization stage.

The sulfur isotopic composition of the sulfides of the second Cu–Co stage splits into two significantly different $\delta^{34}S$ ranges. The first one, which includes most of the measured sulfides, is characterized by $\delta^{34}S$ values (−13.1‰ to +5.2‰; n=15) similar to the $\delta^{34}S$ of the sulfides of the first Cu–Co stage and of the framboidal pyrite (Fig. 8c; Table 1), i.e., consistent with a BSR origin for the sulfur. However, BSR cannot occur at 270–385°C (Machel 2001), the minimum temperature of the fluid of the second Cu–Co stage (cf. El Desouky et al. 2009a). Therefore, it is concluded that this similarity is consistent with remobilization of sulfur from framboidal pyrite and/or from the

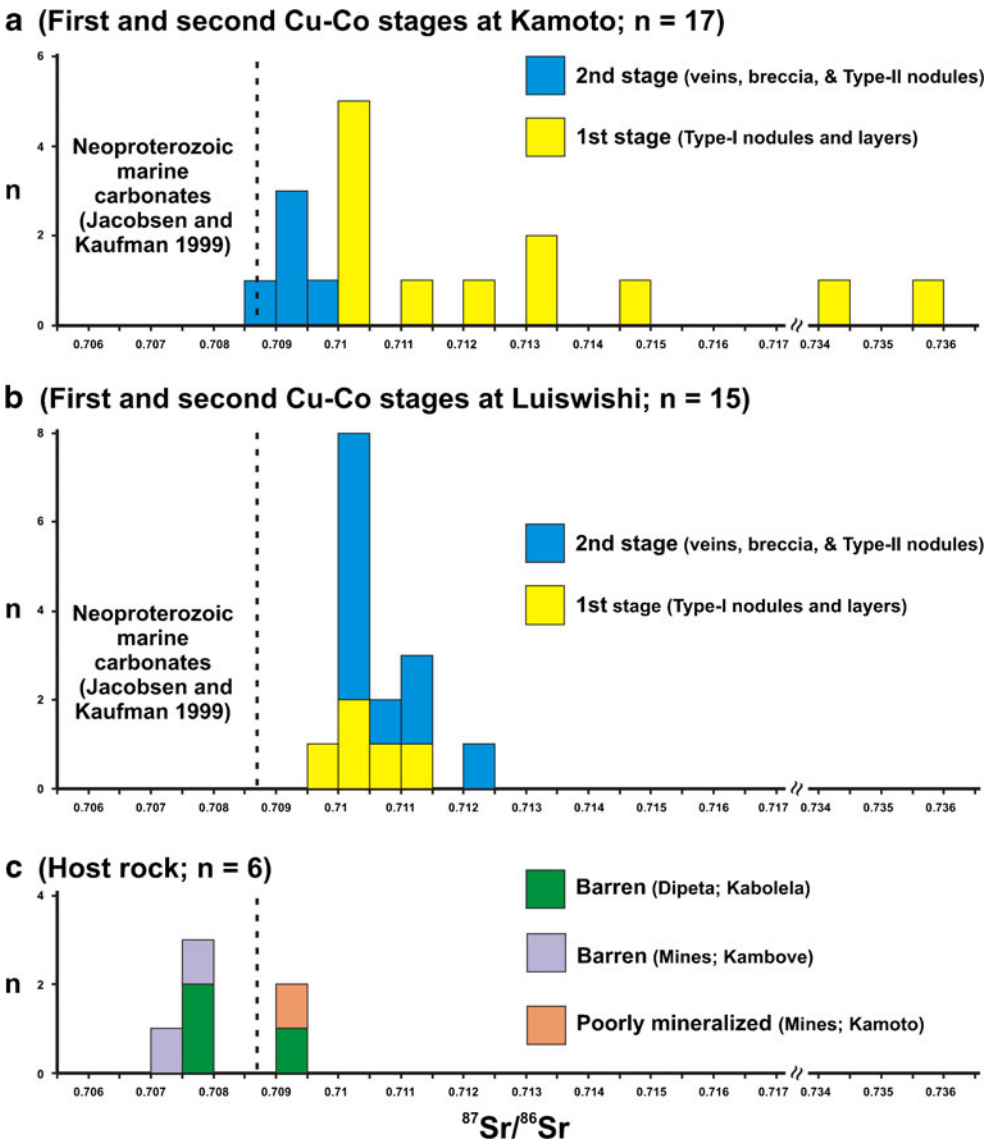

Fig. 10 Histograms showing the distribution of $^{87}Sr/^{86}Sr$ ratios of carbonates. **a**, **b** $^{87}Sr/^{86}Sr$ ratios of dolomites associated with the first (*1st*) and second (*2nd*) Cu–Co stages at Kamoto (**a**) and Luiswishi (**b**). **c** $^{87}Sr/^{86}Sr$ ratios of poorly mineralized/barren host rock carbonates from the Mines Subgroup at Kamoto and Kambove and from the Dipeta Subgroup at Kabolela

sulfides of first Cu–Co mineralization stage during the second one (cf. Wagner and Boyce 2006). The second $\delta^{34}S$ range shows values between +18.6 and +21.0 (n=3; Fig. 8c; Table 1). This heavy sulfur isotope signature, which overlaps with the upper range of mean Neoproterozoic seawater (17.5±3‰), is consistent with thermochemical sulfate reduction at temperatures in excess of 300°C (Harrison and Thode 1957; Kiyosu and Krouse 1990; Machel et al. 1995). There are two possible sources for the sulfates consumed during this TSR process (El Desouky et al. 2009b): (1) relicts of anhydrite in type I nodules and layers (cf. Muchez et al. 2008) and (2) new sulfates imported with the mineralizing/remobilizing fluid of the second Cu–Co stage, possibly originating from the dissolution of the evaporites of the Roan Group (e.g., McGowan et al. 2006). During TSR, H_2S is released and coarse-grained saddle dolomite is often formed as a by-product (Machel 1987a, b, 2001; Machel et al. 1995; Mougin et al. 2007). This H_2S, the early diagenetic sulfides of the first Cu–Co stage, the diagenetic pyrites, and the abundant organic matter within the Mines Subgroup most likely acted as efficient reductants (cf. Hitzman et al. 2005) for the precipitation of the Cu–Co metals during the second Cu–Co stage.

The sulfur isotopic composition of the paragenetically late coarse-grained pyrite of the barren breccia cements (type IV; mean $\delta^{34}S$=14.6‰; n=3; Fig. 8d), which overlaps with the lower range of mean Neoproterozoic seawater (17.5±3‰), is consistent with TSR at a temperature of ≤300°C (cf. Machel et al. 1995). Rather, similar $\delta^{34}S$ signatures (+11‰ to +15‰) were reported for pyrite from the Upper Orebody at Nchanga (McGowan et al. 2003, 2006). The authors related these $\delta^{34}S$ signatures to open-system TSR at temperatures in excess of ~200°C. A heavier $\delta^{34}S$ signature (+22‰ to +23‰) for paragenetically late pyrite in

crosscutting veins was also reported by the same authors and was linked to closed-system TSR.

In contrast to the distinct $\delta^{34}S$ signatures of type I and type IV pyrites, the $\delta^{34}S$ of type II and type III pyrites displays intermediate values (+0.3‰ to +11.3‰; Fig. 8d), for which the interpretation remains speculative. Petrographic observations indicate that type II and type III pyrites are in many places associated with, or replaced, framboidal pyrite (El Desouky 2009). Thus, it is likely that these pyrites, especially the fine-grained type II pyrite, represent a recrystallization product of the diagenetic framboidal pyrite. According to Machel (2001), the most common initial textures of the BSR-related iron sulfides are scattered clusters of framboids, which often tend to recrystallize into more stable forms. If type II and type III pyrite obtained their sulfur only by remobilizing the sulfur of framboidal pyrites, they must have $\delta^{34}S$ values that fall in the wide range of $\delta^{34}S$ of framboidal pyrite, which is not the case. Therefore, the intermediate $\delta^{34}S$ signatures of type II and type III pyrites are likely related to the mixing between light BSR-related sulfur from framboidal pyrite and heavy TSR-related sulfur incorporated during recrystallization of framboidal pyrite (e.g., Wagner et al. 2010). Thus, the $\delta^{34}S$ signature of the new pyrite generation significantly depends on the $\delta^{34}S$ of the parent framboidal pyrite and on the amount of added heavy sulfur during recrystallization (cf. Ohmoto 1986; Hoy and Ohmoto 1989). The $\delta^{34}S$ signatures of late diagenetic to orogenic Cu–Co sulfides from the CACB (see reviews in Selley et al. 2005; Cailteux et al. 2005), which are similar to the intermediate $\delta^{34}S$ signatures of type II and type III pyrites, could be also interpreted to reflect mixing between BSR-related and TSR-related sulfur.

A previous sulfur isotopic study by Lerouge et al. (2005) at Luiswishi yielded $\delta^{34}S$ values between −14.4‰ and +17.5‰ for disseminated, bedding parallel, and stockwork Cu–Co sulfides. Dechow and Jensen (1965) performed a large sulfur isotopic study on the CACB, including samples from the Kamoto principal, which had $\delta^{34}S$ values that range from −15.3‰ to +3.5‰. $\delta^{34}S$ values in the range between −15‰ and +10‰ were also reported for Kamoto by Ohmoto (1986). In general, previous sulfur isotope analyses on Cu–Co sulfides from the CACB display similar wide ranges of $\delta^{34}S$ values that range from −18.4‰ to +23‰ for the Zambian part (Dechow and Jensen 1965; Sweeney et al. 1986; Annels 1989; Sweeney and Binda 1989; McGowan et al. 2003, 2006; Selley et al. 2005) and from −15.3‰ to +18.7‰ for the Congolese part (Dechow and Jensen 1965; Lerouge et al. 2005; Cailteux et al. 2005).

In previous studies in the CACB, there is a common observation that the sulfur isotopic composition of late Cu–Co sulfide generations, e.g., in crosscutting veins, could have $\delta^{34}S$ values which are similar to (e.g., Lerouge et al. 2005) or heavier than (e.g., Annels 1989; McGowan et al 2003, 2006) the early sulfides, i.e., disseminated or nodular Cu–Co sulfides. Furthermore, there is often an agreement that the light $\delta^{34}S$ values are related to bacterial sulfate reduction of seawater sulfate during early diagenesis. However, there are contrasting hypotheses for the origin of the heavy sulfur isotopes, including (1) metamorphic homogenization of original sedimentary $\delta^{34}S$ signatures (Dechow and Jensen 1965), which has been dismissed by McGowan et al. (2003, 2006) for the Nchanga deposit in Zambia, (2) influence of varying paleoenvironmental conditions, e.g., $\delta^{34}S$ values become heavier during regressive events (Sweeney et al. 1986; Sweeney and Binda 1989; Lerouge et al. 2005), (3) addition of heavy sulfide produced at the depositional site by thermochemical sulfate reduction at temperatures >200°C (Ohmoto 1986; Hoy and Ohmoto 1989; McGowan et al. 2003, 2006), and (4) formation of sour gas reservoirs prior to mineralization (Selley et al. 2005).

Carbon and oxygen isotopes

At Kamoto, two samples of the host rock dolomites display $\delta^{13}C$ and $\delta^{18}O$ signatures that overlap with the lower range of Neoproterozoic marine dolomites (−4.0‰ to +4.0‰ for $\delta^{13}C$ and −8‰ to −4‰ for $\delta^{18}O$; Veizer and Hoefs 1976; Lindsay et al. 2005; Fig. 9a). These signatures are in agreement with the marine origin (platform-type carbonates) proposed by Cailteux (1994) for the host rock dolomites of the Mines Subgroup. Most of the remaining host rock dolomite samples show minor depletions from the marine range (~2‰ for $\delta^{18}O$ and <1‰ for $\delta^{13}C$; Fig. 9a). The $\delta^{13}C$ and $\delta^{18}O$ of all the host rock dolomites at Luiswishi and of four samples from Kamoto are depleted by >2.5‰ in $\delta^{18}O$ and by as much as 3.8‰ in $\delta^{13}C$ relative to Neoproterozoic marine dolomites (Fig. 9). The $\delta^{18}O$ depletions of host rock dolomites likely reflect recrystallization under the influence of the hydrothermal fluids of the first and/or the second Cu–Co stages (El Desouky et al. 2009c), whereas the $\delta^{13}C$ depletions could be related to organic matter oxidation during bacterial and/or thermochemical sulfate reduction, or related to normal maturation of organic matter. It is characteristic for dolomites that formed in a marine environment during sedimentation and early diagenesis to be partly or completely recrystallized and depleted in $\delta^{18}O$ and/or $\delta^{13}C$ during burial and hydrothermal fluid flow (e.g., Smith and Dorobek 1993; Nielsen et al. 1994; Hitzman and Beaty 1996).

Based on the sulfur isotope data, the fine-grained dolomite associated with the sulfides of the first Cu–Co stage in type I nodules and layers is interpreted as by-product of bacterial sulfate reduction during early diagenesis, i.e., formed at temperatures below 80°C

(Machel 2001). Considering this maximum temperature and assuming that this dolomite precipitated from a fluid with a $\delta^{18}O$ in the range of Neoproterozoic seawater ($\delta^{18}O$=−2±1‰ V-SMOW; Hudson and Anderson 1989), the minimum $\delta^{18}O$ value for this dolomite can be calculated (−12.9‰ V-PDB) using the fractionation factors published by O'Neil et al. (1969). All the $\delta^{18}O$ values of the dolomite samples in type I nodules and layers at both Kamoto and Luiswishi, except one sample (Kamoto sample KA05VD052; $\delta^{18}O$=−14.13‰; Table 2), are higher than the calculated minimum $\delta^{18}O$ value (i.e., more than −12.9‰ V-PDB; Fig. 9; Tables 2 and 3), confirming their origin as by-products of BSR.

According to Machel et al. (1995), the authigenic carbonates that formed as by-products of BSR could obtain their carbon from two principal sources: very light organic carbon released from oxidation of organic matter or hydrocarbons and inorganic carbon, with a marine $\delta^{13}C$ signature. The $\delta^{13}C$ signature of the generated carbonate mineral will thus depend on the relative proportion of these two carbon sources. The dolomite associated with the first Cu–Co stage at both Kamoto and Luiswishi display $\delta^{13}C$ values that are either depleted (down to −9.9‰) or similar to the $\delta^{13}C$ signature of Neoproterozoic marine dolomites (Fig. 9; Tables 2 and 3). The $\delta^{13}C$ depleted dolomite reflects incorporation of organic carbon from the oxidation of organic matter during BSR (cf. Irwin et al. 1977; Machel et al. 1995). There are two possible explanations for the nondepleted $\delta^{13}C$ dolomite. Firstly, during dolomite precipitation, inorganic carbon was dominant and there was little or no organic carbon generated (Machel et al. 1995). For example, BSR-related carbonates with a marine $\delta^{13}C$ signature at Pine Point (Canada) have been explained in this way (Macqueen and Powell 1983; Machel et al. 1995). Secondly, the original isotopic signature of the dolomite has been overprinted by recrystallization in excess of inorganic carbon, possibly during the migration of the fluid of the second Cu–Co stage. The latter explanation is especially favored for the samples with very low $\delta^{18}O$ values, e.g., sample KA05VD052 (Table 2).

The coarse-grained dolomite associated with the sulfides of the second Cu–Co stage displays a wide range of $\delta^{13}C$ and $\delta^{18}O$ values that mostly overlap with the signatures of the earlier dolomite generations (i.e., those of the host rock and type I nodules and layers) or are significantly depleted (Fig. 9). The similarity of the oxygen isotopic composition of the coarse-grained dolomites and of surrounding earlier dolomite generations is consistent with carbonate precipitation from a fluid in which its oxygen isotopic composition was buffered by the host sediments (Gray et al. 1991; Marquer and Burkhard 1992; Muchez et al. 1995; Kenis et al. 2000; Verhaert et al. 2009). This isotopic similarity confirms the possible recrystallization of earlier dolomite generations as suggested earlier. Recrystallization was likely more significant at Luiswishi than at Kamoto.

The coarse-grained quartz, which formed immediately before the coarse-grained dolomite of the second Cu–Co stage, precipitated from a fluid with a temperature of 270–320°C at Kamoto and of 300–385°C at Luiswishi (El Desouky et al. 2009a). Most of the coarse-grained dolomite samples from both Luiswishi and Kamoto have $\delta^{18}O$ values that range between −15.0‰ and −11.2‰ (Fig. 9). These values indicate precipitation from a fluid with a $\delta^{18}O$ value between 7.8‰ and 11.7‰ V-SMOW at a temperature of 300°C (dolomite–water fractionation equation given by Land 1983). This fluid was enriched by 9.8‰ to 13.7‰ in heavy O relative to Neoproterozoic seawater ($\delta^{18}O$=−2±1‰ V-SMOW; Hudson and Anderson 1989). This large shift is likely related to significant water–rock interaction (Sheppard 1986). At 300°C, the minimum $\delta^{18}O$ values of coarse-grained dolomite at Kamoto (−24.0‰; Fig 9a; Table 2) and Luiswishi (−19.0‰; Fig 9b; Table 3) reflect precipitation from a fluid with a maximum $\delta^{18}O$ value between −1.4‰ and 3.7‰, respectively (cf. Land 1983). A similar wide range of $\delta^{18}O$ values (−1‰ to +8‰) was reported by McGowan et al. (2006) for the fluid in equilibrium with quartz and dolomite veins in the Nchanga deposit (Zambian Copperbelt; Fig. 2).

Based on the sulfur isotope data, at least part of the coarse-grained dolomite associated with the sulfides of the second Cu–Co stage formed as a by-product of thermochemical sulfate reduction. There are two possible explanations for the light $\delta^{13}C$ values of these dolomites. Firstly, preferential incorporation of light organic carbon generated from the oxidation of organic matter during TSR (cf. Irwin et al. 1977; Machel et al. 1995). Indeed, a TSR-related $\delta^{34}S$ signature of +18.6‰ to +19.4‰ (Table 1) is obtained from the Cu–Co sulfides of the vein (sample LS06HA108) that shows the lowest $\delta^{13}C$ value (−8.61‰; Fig. 9b; Table 3). Secondly, incorporation of light organic carbon obtained from the interaction between the dolomitizing fluid and the earlier, $\delta^{13}C$ depleted, dolomite generations of type I nodules and layers and/or the host rock.

The paragenetically late Fe-rich dolomite at both Luiswishi and Kamoto display a consistent $\delta^{13}C$ signature (−3.8‰ to −1‰; Tables 2 and 3) that agrees with the lower range of Neoproterozoic marine dolomites (Veizer and Hoefs 1976; Lindsay et al. 2005), however, with a significantly depleted $\delta^{18}O$ signature (mean=−19.7‰; Fig. 9). This $\delta^{18}O$ value could be related to carbonate precipitation from a high-temperature hydrothermal fluid postdating the second Cu–Co stage (El Desouky et al. 2009c) or from lower temperature meteoric fluids.

Previous C–O isotopic studies in the Zambian Copperbelt yielded $\delta^{13}C$ and $\delta^{18}O$ values similar to those obtained for Luiswishi and Kamoto in the Katanga Copperbelt. At

the Nchanga deposit (Zambia; Fig. 2), the dolomite that is assumed to be of marine origin has an oxygen isotopic composition that varies from −8.2‰ to −7.6‰ V-PDB and a carbon isotopic composition of +1.4‰ to +2.5‰ V-PDB (McGowan et al. 2006). These values partly overlap with the range of Neoproterozoic marine dolomites (Veizer and Hoefs 1976; Lindsay et al. 2005) and are similar to the values obtained from the host rock dolomites at Kamoto (Fig. 9a). However, dolomite in shear zones and alteration zones from the Upper Orebody, at Nchanga, has $\delta^{18}O$ values that vary from −18.6‰ to −13.6‰ V-PDB and $\delta^{13}C$ values that fall between +2.9‰ and −8.3‰ (McGowan et al. 2006). These values are similar to the values obtained from the coarse-grained dolomite associated with the syn-orogenic sulfides of the second Cu–Co stage at both Luiswishi and Kamoto. Similarly to our interpretation, McGowan et al. (2006) suggested that this dolomite formed as a reaction product of in situ thermochemical sulfate reduction of an oxidized, sulfate-rich, high-temperature fluid. The authors also proposed that the Cu–Co mineralization at Nchanga formed during basin inversion at the onset of the Lufilian Orogeny.

Selley et al. (2005) reviewed previous C–O isotopic studies of the Zambian Copperbelt (Annels 1989; Sweeney and Binda 1989) and performed an extensive isotopic study on 369 carbonate samples (whole rock, veins, and evaporite nodules) from ten deposits. The $\delta^{13}C$ and $\delta^{18}O$ values range between values typical of Neoproterozoic marine carbonates in the unaltered sedimentary carbonates and the carbonates in the barren gaps to isotopically light values ($\delta^{13}C$=−26‰ to −4.0‰ V-PDB and $\delta^{18}O$=−25‰ to −7.6‰ V-PDB) for samples within or close to the mineralization. This wide range of $\delta^{18}O$ values is consistent with the $\delta^{18}O$ signatures reported at Luiswishi and Kamoto for the fine-grained and coarse-grained dolomites associated with the first and second Cu–Co stages, respectively, and for the postdating Fe-rich dolomites. However, the $\delta^{13}C$ values of the carbonates from Luiswishi and Kamoto only overlap with the upper part of the wide range of $\delta^{13}C$ values reported by Selley et al. (2005). Selley et al. (2005) observed that most of the samples with >100 ppm Cu have low $\delta^{13}C$ values. Based on this trend, the authors suggested that metal deposition was mainly controlled by reduction–oxidation reactions, i.e., former organic matter (evidenced by low $\delta^{13}C$ values) facilitated reduction of sulfate to H_2S, resulting in copper sulfide precipitation. Existing data and our present study highlight the role of H_2S generated by BSR and/or TSR in reducing the Cu–Co metals from hydrothermal oxidized fluids and the influence of both organic carbon and the temperature of the mineralizing/remobilizing fluids in the $\delta^{13}C$ and $\delta^{18}O$ signatures of the carbonate minerals associated with the Cu–Co mineralization.

Rb–Sr isotopes

The $^{87}Sr/^{86}Sr$ ratios of four barren host rock carbonate samples from both the Mines and Dipeta Subgroups at Kambove and Kabolela fall into a narrow range (0.70723 to 0.70796; Table 4) that overlaps with the Sr isotopic composition of Neoproterozoic marine carbonates ($^{87}Sr/^{86}Sr$=0.7056 to 0.7087; Jacobsen and Kaufman 1999; Fig. 10c). The $^{87}Sr/^{86}Sr$ ratios of one barren host rock carbonate sample from the Dipeta Subgroup at Kabolela (sample KB08HA3; 0.70927; Table 4) and the poorly mineralized host rock sample from the Mines Subgroup at Kamoto (sample KA05VD081; 0.70904; Table 4) are slightly more radiogenic than the Neoproterozoic seawater signature (Fig. 10c). Correcting these two ratios for in situ decay of ^{87}Rb for an age of 800 Ma, a median value for the age range of the Roan Group (≤880 to ≥735 Ma; Armstrong et al. 2005; Key et al. 2001; Fig. 3a), yields $^{87}Sr/^{86}Sr$ values (0.70898 for sample KB08HA3 and 0.70849 for sample KA05VD081) that overlap with the Neoproterozoic seawater signature.

At Kamoto, the fine-grained dolomite associated with the sulfides of the first Cu–Co stage displays a wide range of $^{87}Sr/^{86}Sr$ ratios (0.71012 to 0.73576) that is significantly more radiogenic than the $^{87}Sr/^{86}Sr$ range of Neoproterozoic marine carbonates (Table 4; Fig. 10a). The $^{87}Sr/^{86}Sr$ ratios (0.70987 to 0.71104) of dolomite associated with the first Cu–Co stage at Luiswishi are also more radiogenic than Neoproterozoic marine carbonates (Table 4; Fig. 10b), but their mean $^{87}Sr/^{86}Sr$ of 0.71050 is lower than the mean $^{87}Sr/^{86}Sr$ value at Kamoto (0.71548). These $^{87}Sr/^{86}Sr$ ratios are also significantly more radiogenic than the $^{87}Sr/^{86}Sr$ ratios recorded from the poorly mineralized and barren host rock carbonates of the Mines and Dipeta Subgroups at Kamoto, Kambove, and Kabolela (Fig. 10; Table 4). This suggests that the radiogenic Sr signature of the fine-grained dolomite is related to the Cu–Co mineralization. The $^{87}Rb/^{86}Sr$ and $^{87}Sr/^{86}Sr$ ratios of fine-grained dolomites from both Luiswishi and Kamoto are not correlated (El Desouky 2009). There is also no correlation between $^{87}Sr/^{86}Sr$ ratios and Sr elemental content (ca. 2–42 ppm; Table 4) in a Sr mixing diagram (Fig. 11a). These observations indicate that the radiogenic $^{87}Sr/^{86}Sr$ values are unrelated to significant in situ decay of ^{87}Rb. Indeed, no significant changes occur if the $^{87}Sr/^{86}Sr$ ratios of the fine-grained dolomites are corrected for in situ decay of ^{87}Rb even for an age of 816 Ma (Table 4). Thus, the radiogenic Sr was most likely introduced by the mineralizing fluid of the first Cu–Co stage from an external radiogenic source. Ngoyi et al. (1991) presented some whole-rock Rb–Sr data from the granitic basement exposed at the Luina Dome (DRC; Fig. 2). The $^{87}Sr/^{86}Sr$ ratios of these samples (n=10) vary between 0.733 and 0.895, with one very radiogenic value of 1.408. Similar to the fine-grained dolomite, the

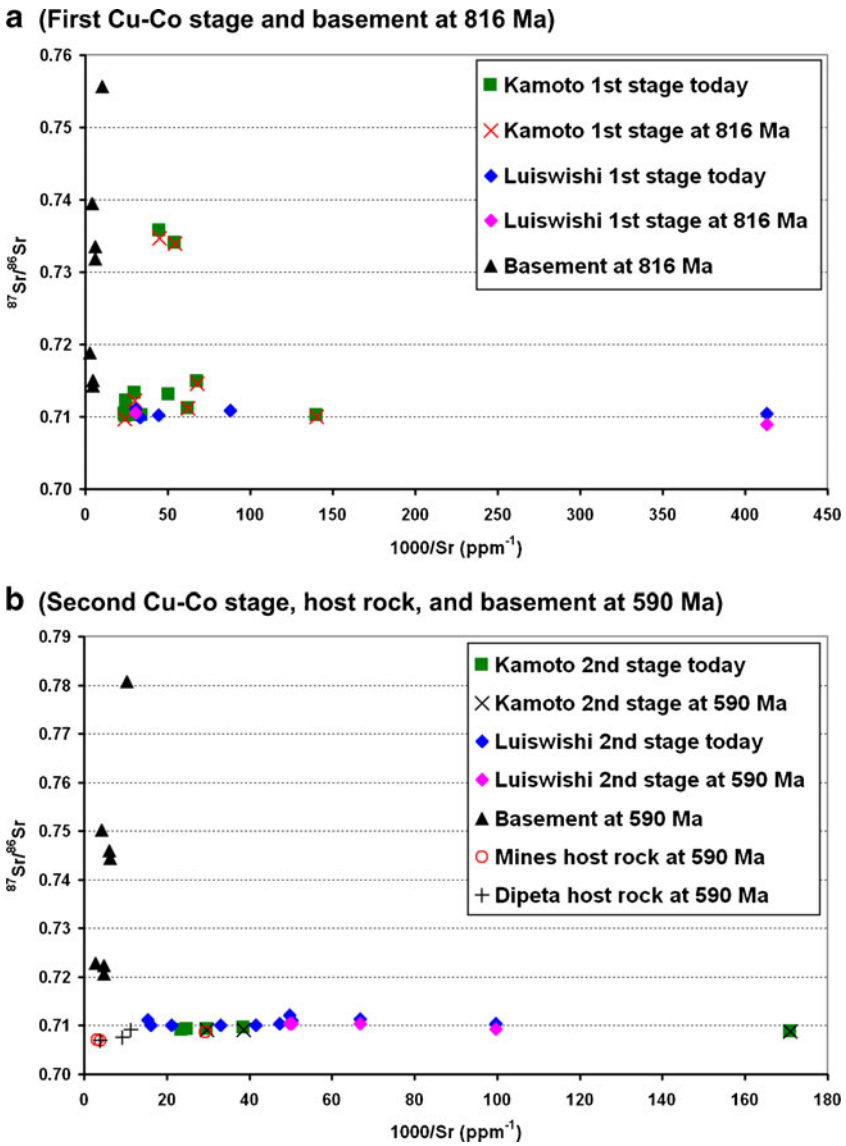

Fig. 11 $^{87}Sr/^{86}Sr$ vs. 1,000/Sr mixing diagrams. **a** Mixing diagram for dolomites associated with the first (*1st*) Cu–Co stage at Kamoto and Luiswishi in comparison with the basement in the Luina Dome (DRC; Ngoyi et al. 1991), with $^{87}Sr/^{86}Sr$ ratios recalculated to 816 Ma. **b** Mixing diagram for dolomites associated with the second (*2nd*) Cu–Co stage at Kamoto and Luiswishi in comparison with poorly mineralized/barren host rock carbonates and the basement, with $^{87}Sr/^{86}Sr$ ratios recalculated to 590 Ma

$^{87}Sr/^{86}Sr$ ratios of seven basement samples were recalculated to 816 Ma, a Re–Os age obtained from chalcopyrite in the hanging wall at the Konkola deposit, near the Luina Dome (Selley et al. 2005). This is the oldest age published for the Cu–Co ore deposits in the CACB and in agreement with an early diagenetic origin of the mineralization (Selley et al. 2005). The fine-grained dolomite and the granitic basement show a good correspondence in a $^{87}Sr/^{86}Sr$ vs. 1,000/Sr mixing diagram (Fig. 11a). This indicates that the basement was most likely an important source for the radiogenic Sr and that the mineralizing fluid of the first Cu–Co stage has interacted with the underlying basement rocks and/or with arenitic Lower Roan sedimentary rocks derived from such a basement (El Desouky et al. 2009c). Similarly, Annels (1989) proposed a significant interaction between Cu–Co mineralizing fluids and the basement, along major fault systems in the Zambian Copperbelt. These suggestions are consistent with the hypotheses that relate the source of metals in the CACB to the underlying basement (e.g., Sweeney et al. 1991; Cailteux et al. 2005).

The $^{87}Sr/^{86}Sr$ signatures of the coarse-grained dolomite associated with the sulfides of the second Cu–Co stage are more radiogenic (0.70883 to 0.71215; Table 4) than Neoproterozoic marine carbonates but much less radiogenic than the dolomites associated with the first Cu–Co stage (Fig. 10a, b). The $^{87}Rb/^{86}Sr$ and $^{87}Sr/^{86}Sr$ ratios of these dolomites display some correlation (El Desouky 2009). Consequently, when these $^{87}Sr/^{86}Sr$ ratios are corrected for in situ decay of ^{87}Rb for an age of 590 Ma, the age of the onset of the Lufilian Orogeny (Rainaud et al. 2005), rather significant changes occurred especially on the Luiswishi samples, e.g., sample LS06HA037 ($^{87}Sr/^{86}Sr$ changes from 0.71215 to 0.71034; Table 4). The $^{87}Sr/^{86}Sr$ values of the granitic basement and of the poorly mineralized/barren host

rock carbonates were also corrected for in situ decay of ^{87}Rb for an age of 590 Ma (Table 4). In a $^{87}Sr/^{86}Sr$ vs. 1,000/Sr mixing diagram, the coarse-grained dolomite of the second Cu–Co stage shows a better correspondence with the host rocks than with the granitic basement rocks (Fig. 11b). This suggests that the high-temperature, high-salinity fluid of the second Cu–Co stage has significantly interacted with the country rocks of the Roan Group (El Desouky et al. 2009c). Based on the similarity in sulfide types between veins and host rocks, the sulfur isotopic signature of the sulfides of the second Cu–Co stage, and on the Sr isotopic data, it is concluded that the fluid of the second Cu–Co stage was likely a remobilizing fluid that formed high-grade ore deposits in the Katanga Copperbelt and likely did not mobilize additional metals from the basement rocks. However, the addition of metals from other sources, e.g., the mafic rocks within the upper part of the Roan Group, is not excluded and requires further investigation. The good correspondence between the Sr isotope signature of the dolomite of the second Cu–Co stage and the barren host rock carbonates of the Dipeta Subgroup at 590 Ma (Fig. 11b) is in agreement with the hypothesis that relate the salinity of the late Cu–Co mineralizing/remobilizing fluids in the CACB to the dissolution of the former evaporites within the Roan Group (Selley et al. 2005; McGowan et al. 2006; Heijlen et al. 2008; El Desouky et al. 2009a).

Summary and mineralization models

Two main hypogene Cu–Co sulfide stages and associated gangue minerals (dolomite and quartz) were distinguished in the Katanga Copperbelt (DRC), the Congolese part of the well-known CACB. The first is an early diagenetic, typical stratiform mineralization with fine-grained minerals, whereas the second is a multistage syn-orogenic stratiform to stratabound mineralization with coarse-grained minerals. The main hypogene Cu–Co sulfide minerals of the two stages are chalcopyrite, bornite, carrollite, and chalcocite. The proportions of these sulfide minerals and of their associated gangue minerals may vary significantly between deposits and between different layers within the Mines Subgroup. The hypogene minerals of the first and second Cu–Co stages are in many places replaced by supergene sulfides (e.g., digenite and covellite), especially near the surface, and are completely oxidized in the weathered superficial zone and in surface outcrops, with malachite, heterogenite, chrysocolla, and azurite as the main Cu–Co oxidation products. The supergene Cu–Co oxide minerals are mainly concentrated along cracks and in the fracture zones associated with faults. This reflects the role of tectonic structures and surface/near-surface processes in leaching, remobilizing, and upgrading the primary mineralization.

Results of S, C, O, and Sr isotope analyses performed on the different sulfide and carbonate generations combined with fluid inclusion microthermometric data from El Desouky et al. (2009a) can be integrated in two main mineralization models, i.e., an early diagenetic hydrothermal model for the first Cu–Co stage (Fig. 12a) and a syn-orogenic hydrothermal model for the second stage (Fig. 12b). The first model proposes that an evaporated seawater (salinity=11.3 to 20.9 wt.% NaCl equiv; El Desouky et al. 2009a) of Roan age (likely >ca. 816 Ma; cf. Selley et al. 2005) migrated downward (Fig. 12a). Migration through the deeper subsurface allowed the fluid to obtain its temperature (115°C to ≤220°C; El Desouky et al. 2009a) and to interact with the basement rocks (Fig. 12a). This interaction has enriched the fluid with radiogenic strontium and most likely with Cu–Co metals. The abundant organic matter and evaporite nodules and layers in the sediments of the Mines Subgroup allowed BSR to take place during early diagenesis. BSR caused the release of H_2S and the replacement of evaporites by dolomite (Muchez et al. 2008). The oxidized mineralizing fluid was then expelled upward, possibly along major basin and/or subbasin fault systems (e.g., Annels 1989; Selley et al. 2005), into the overlying sedimentary sequences of the Roan Group (Fig. 12a). The sediments of the Mines Subgroup were the first and the most reducing (Cailteux 1994) unit infiltrated by the fluid. Cu and Co reacted with the H_2S produced by BSR to precipitate Cu–Co sulfides in the nodules and disseminated in the host rock (Muchez et al. 2008). Lateral fluid migration into the Mines Subgroup was likely promoted by the primary porosity of the sediments during early diagenesis (e.g., Annels 1989). The so-called barren gaps have likely been formed due to abrupt lateral paleoenvironmental lithofacies variations (Cailteux et al. 2005; Selley et al. 2005), which have limited the availability of reductants and/or sulfur in host rocks and/or disturbed the lateral fluid migration (Fig. 12a). This model is supported by three independent data sets: (1) the sulfur isotope signature obtained from the sulfides of the first Cu–Co stage (−10.3‰ to +3.1‰ V-CDT) partly overlaps with the $\delta^{34}S$ signature of framboidal pyrite (−28.7‰ to 4.2‰V-CDT) in agreement with a BSR origin for the sulfides of the first Cu–Co stage, (2) the depleted C (−9.9‰ to −1.4‰ V-PDB) and O (−14.3‰ to −7.7‰ V-PDB) isotope signatures of the fine-grained dolomites associated with the sulfides of the first Cu–Co stage agree with a BSR origin, and (3) the significantly radiogenic Sr isotope signature ($^{87}Sr/^{86}Sr$= 0.70987 to 0.73576) obtained from the fine-grained dolomite corresponds well with the Sr isotope signature of the granitic basement at 816 Ma, the oldest age published for the Cu–Co ore deposits in the CACB (Selley et al. 2005).

The second model suggests that a deep burial fluid, possibly of evaporated marine origin, migrated through the thick sedimentary sequence of the Katanga Supergroup

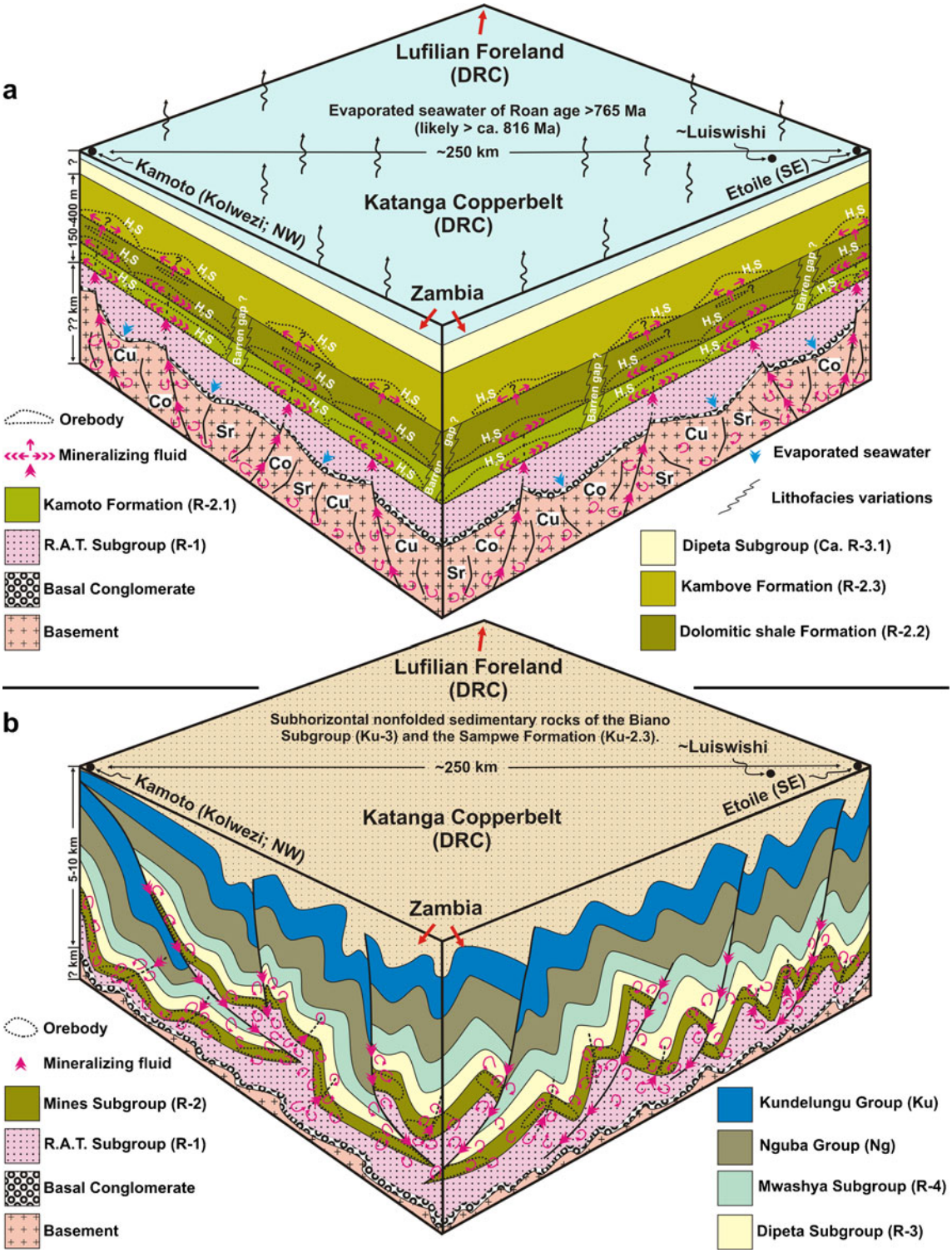

Fig. 12 3D schematic diagrams illustrating **a** the early diagenetic hydrothermal model for the origin of the typical stratiform mineralization of the first Cu–Co stage and **b** the syn-orogenic hydrothermal model for the origin of the second Cu–Co stage in the Katanga Copperbelt. See text for explanations and Fig. 3 for the stratigraphic units. The location of ore deposits, barren gaps, and faults are imaginary. The deformation pattern in **b** is inspired from the cross sections of Jackson et al. (2003)

during late burial and the Lufilian Orogeny. Fluid migration and circulation through the host rocks was likely facilitated by the orogenic structures, e.g., the brecciated zones along faults and between the megabreccia blocks. The fluid, which obtained its high temperature (>270°C; El Desouky et al. 2009a) by deep migration, significantly interacted with the sediments of the Roan Group (Fig. 12b). There is yet no evidence in the Katanga Copperbelt that this fluid has interacted with the basement rocks. The salinity of the fluid significantly increased (35–45.5 wt.% NaCl equiv; El Desouky et al. 2009a), likely via the dissolution of the Roan Group evaporites, e.g., those of the Dipeta Subgroup (e.g., McGowan et al. 2006; El Desouky et al. 2009a). Interaction with the sediments allowed the fluid to increase its $\delta^{18}O$ (up to 11.7‰ V-SMOW) by intense water–rock interaction; to acquire its Sr isotope signature ($^{87}Sr/^{86}Sr$= 0.70883 to 0.71215), which shows a good correspondence with the $^{87}Sr/^{86}Sr$ ratios (0.70723 to 0.70927) of poorly mineralized/barren host rocks from the Mines and Dipeta Subgroups at 590 Ma, the onset of the Lufilian Orogeny; and to leach and remobilize significant amounts of Cu and Co, likely from the stratiform sulfides of the first Cu–Co stage. The sulfides of the second Cu–Co stage are characterized by $\delta^{34}S$ signatures, which are either similar (−13.1‰ to +5.2‰ V-CDT) to the $\delta^{34}S$ values of the sulfides of the first Cu–Co stage, or comparable (+18.6‰ to +21.0‰ V-CDT) to the $\delta^{34}S$ of Neoproterozoic seawater. This indicates that sulfur was obtained by remobilization from the first stage and from TSR at temperatures in excess of 300°C. H_2S, generated by TSR, the diagenetic sulfides of the first Cu–Co stage, the diagenetic pyrites, and the abundant organic matter within the Mines Subgroup most likely acted as efficient reductants (cf. Hitzman et al. 2005) for the Cu and Co dissolved in the oxidized high-temperature, high-salinity fluid of the second Cu–Co stage.

Acknowledgments We would like to thank the Forrest International Group (G.F.I.) and Compagnie Minière du Sud Katanga (C.M.S.K.) for access to the Luiswishi mine and for the availability of samples. The geologists and workers of the Forrest International Group are thanked for their cooperation during sampling and mine visit. Thanks to Herman Nijs for the careful preparation of numerous thin and polished sections. Thanks to Eric Pirard (University of Liège, Belgium) for the permission to sample the Kamoto borehole F120. The barren host rock carbonate samples of Kambove and Kabolela were collected from the rock collections of the Royal Museum for Central Africa (RMCA, Tervuren, Belgium). We are grateful to Michael Joachimski (University of Erlangen, Germany) for performing the C–O isotope analyses. The paper has benefited from constructive comments by Sharad Master, an anonymous reviewer, the Associate Editor Hartwig Frimmel, and the Editor-in-Chief Bernd Lehmann. The Katholieke Universiteit Leuven is thanked for financing the Ph.D. research of Hamdy El Desouky, through the Development Co-operation Scholarships Programme. This research is also financially support by the research grants number G.0585.06 and G.0414.08 from the FWO-Vlaanderen (Belgium).

References

Annels AE (1989) Ore genesis in the Zambian Copperbelt with particular reference to the northern sector of the Chambishi basin. In: Boyle RW, Brown AC, Jefferson CW, Jowett EC, Kirkham RV (eds) Sediment-hosted stratiform copper deposits. Geol Ass Canada, Spec Pap 36. Geological Association of Canada, St. John's, pp 427–452

Armstrong RA, Master S, Robb LJ (2005) Geochronology of the Nchanga Granite, and constraints on the maximum age of the Katanga Supergroup, Zambian Copperbelt. J Afr Earth Sci 42:32–40

Bartholomé P (1974) On the diagenetic formation of ores in sedimentary beds, with special reference to Kamoto, Shaba, Zaïre. In: Bartholomé P (ed) Gisements Stratiformes et Provinces Cuprifères. Centenaire de la Société Géologique de Belgique, Liége, pp 203–213

Bartholomé P, Katekesha F, Lopez-Ruiz J (1971) Cobalt zoning in microscopic pyrite from Kamoto, Republic of the Congo. Miner Deposita 6:167–176

Bartholomé P, Evrard P, Katekesha F, Lopez-Ruiz J, Ngongo M (1972) Diagenetic ore-forming processes at Kamoto, Katanga, Republic of the Congo. In: Amstutz GC, Bernard AJ (eds) Ores in sediments. Springer, Heidelberg, pp 21–41

Bateman AM (1930) Ores of the North Rhodesian Copperbelt. Econ Geol 25:365–418

Batumike MJ, Cailteux JLH, Kampunzu AB (2007) Lithostratigraphy, basin development and regional correlations of the Neoproterozoic Nguba and Kundelungu rock successions, central African Copperbelt. Gondwana Res 11:432–447

Binda PL, Porada H (1995) Observations on the Katangan breccias of Zambia. In: Wendorff M, Tack L (eds) Late Proterozoic Belts in Central and Southwestern Africa. IGCP Project 302. Ann Sci Géol 101. Musée Royal de l'Afrique Centrale, Tervuren, pp 49–62

Birck JL (1986) Precision K–Rb–Sr isotopic analysis—application to Rb–Sr chronology. Chem Geol 56:73–83

Brems D, Muchez Ph, Sikazwe O, Mukumba W (2009) Metallogenesis of the Nkana copper–cobalt South Orebody, Zambia. J Afr Earth Sci 55:185–196

Cailteux J (1994) Lithostratigraphy of the Neoproterozoic Shaba type (Zaire) Roan Supergroup and metallogenesis of associated stratiform mineralization. J Afr Earth Sc 19:279–301

Cailteux J, Kampunzu AB (1995) The Katangan tectonic breccias in the Shaba province (Zaire) and their genetic significance. In: Wendorff M, Tack L (eds) Late Proterozoic Belts in Central Africa. Ann Sci Géol 101. Musée Royal de l'Afrique Centrale, Tervuren, pp 63–76

Cailteux JLH, Kaputo AK, Kampunzu AB (2003) Structure, lithostratigraphy and Cu–Co mineralization of the Mines Subgroup at Luiswishi, central Africa Copperbelt. In: Cailteux J (ed) Proterozoic sediment-hosted base metal deposits of Western Gondwana, Lubumbashi, pp 103–107

Cailteux JLH, Kazadi MB, Lerouge C, Kampunzu AB (2004) Luiswishi Cu–Co stratiform deposit (D.R. Congo): structural, sedimentary and base metal setting. Proceedings of the Geosciences Africa 2004, University of the Witwatersrand, Johannesburg, South Africa, Abstract vol. 1, pp 97–98

Cailteux JLH, Kampunzu AB, Lerouge C, Kaputo AK, Milesi JP (2005) Genesis of sediment-hosted stratiform copper–cobalt deposits, central African Copperbelt. J Afr Earth Sci 42:134–158

Cailteux JLH, Kampunzu AB, Lerouge C (2007) The Neoproterozoic Mwashya–Kansuki sedimentary rock succession in the central African Copperbelt, its Cu–Co mineralization, and regional correlations. Gondwana Res 11:414–431

Canfield DE (2001) Isotope fractionation by natural populations of sulfate-reducing bacteria. Geochim Cosmochim Acta 65:1117–1124

Chávez WX Jr (2000) Supergene oxidation of copper deposits: zoning and distribution of copper oxide minerals. Soc Econ Geol Newsl 41:9–21

Claypool GE, Holser WT, Kaplan IR, Sakai H, Zak I (1980) The age curves of sulphur and oxygen isotopes in marine sulphate and their mutual interpretation. Chem Geol 28:199–260

Daly MC, Chakroborty SK, Kasolo P, Musiwa M, Mumba P, Naidu B, Namateba C, Ngambi O, Coward MP (1984) The Lufilian arc and Irumide belt of Zambia: results of a geotraverse across their intersection. J Afr Earth Sci 2:311–316

Davidson CM (1931) The geology and ore deposits of Chambishi, northern Rhodesia. Econ Geol 26:131–154

Dechow E, Jensen ML (1965) Sulphur isotopes of some central African sulfide deposits. Econ Geol 60:894–941

De Magnée I, François A (1988) The origin of the Kipushi (Cu, Zn, Pb) deposit in direct relation with a Proterozoic salt diapir. Copperbelt of Central Africa, Shaba, Rep. of Zaïre. In: Friedrich GH, Herzig PM (eds) Base metal sulfide deposits. Springer, Heidelberg, pp 74–93

Deniel C, Pin C (2001) Single-stage method for the simultaneous isolation of lead and strontium from silicate samples for isotopic measurements. Anal Chim Acta 426:95–103

De Putter T, Dewaele S, Decrée S, Jedwab J (2008) Caractérisation géochimique des minerais de cuivre et cobalt de l'Arc Cuprifère katangais (République Démocratique du Congo) et implications génétiques. Proceedings, 22ème Réunion des Sciences de la Terre, Collogue De Launay, Nancy, France, 21–24th April 2008, p 554

Dewaele S, Muchez Ph, Vets J, Fernandez-Alonzo M, Tack L (2006) Multiphase origin of the Cu–Co ore deposits in the western part of the Lufilian fold-and-thrust belt, Katanga (Democratic Republic of Congo). J Afr Earth Sci 46:455–469

Dickson JAD (1966) Carbonate identification and genesis revealed by staining. J Sediment Petrol 36:491–505

El Desouky HA (2009) Metallogenesis of stratiform copper deposits in the Lufilian Orogen, Democratic Republic Congo. Unpublished Ph.D. thesis, Katholieke Universiteit Leuven, Belgium, 210pp

El Desouky H, Haest M, Muchez Ph, Dewaele S, Cailteux J, Heijlen W (2007a) Fluid evolution in the Katanga Copperbelt, Democratic Republic of Congo. In: Andrew CJ et al (eds) Digging deeper. Proceedings of the 9th Biennial SGA Meeting. Irish Association for Economic Geology, Dublin, pp 213–216

El Desouky HA, Muchez Ph, Dewaele S, Boutwood A, Tyler R (2007b) The stratiform copper mineralization of the Lufukwe anticline, Lufilian foreland, Democratic Republic Congo. Geol Belg 10:148–151

El Desouky HA, Muchez Ph, Dewaele S, Boutwood A, Tyler R (2008a) Postorogenic origin of the stratiform Cu mineralization at Lufukwe, Lufilian foreland, Democratic Republic Congo. Econ Geol 103:555–582

El Desouky H, Muchez Ph, Boyce A, Cailteux J, Dewaele S (2008b) Evidence for two main Cu–Co mineralization phases in the Katanga Copperbelt, DRC. In: Africa Uncovered Mineral Resources for the future—proceedings of the Joint Conference of the Society of Economic Geologists (SEG) and the Geological Society of South Africa (GSSA), Johannesburg, South Africa, pp 234–237

El Desouky HA, Muchez Ph, Tyler R (2008c) The sandstone-hosted stratiform copper mineralization at Mwitapile and its relation to the mineralization at Lufukwe, Lufilian foreland, Democratic Republic Congo. Ore Geol Rev 34:561–579

El Desouky HA, Muchez Ph, Cailteux J (2009a) Two Cu–Co sulfide phases and contrasting fluid systems in the Katanga Copperbelt, Democratic Republic of Congo. Ore Geol Rev 36:315–332

El Desouky H, Muchez Ph, Boyce A, Cailteux J, Dewaele S (2009b) Sources of sulphur in the Katanga Copperbelt, Democratic Republic of Congo. In: Williams PJ et al (eds) Smart science for exploration and mining. Proceedings of the 10th Biennial SGA Meeting, James Cook University, Economic Geology Research Unit, Townsville, Australia. Millbank, Rotterdam, pp 432–434

El Desouky H, Muchez Ph, Schneider J, Cailteux J (2009c) Stable (C–O) and radiogenic (Sr) isotope geochemistry of the Luiswishi and Kamoto Cu–Co ore deposits, Katanga Copperbelt, Democratic Republic of Congo. In: Williams PJ et al (eds) Smart science for exploration and mining. Proceedings of the 10th Biennial SGA Meeting, James Cook University, Economic Geology Research Unit, Townsville, Australia. Millbank, Rotterdam, pp 435–437

Fallick AE, McConville P, Boyce AJ, Burgess R, Kelley SP (1992) Laser microprobe stable isotope measurements on geological-materials—some experimental considerations (with special reference to Delta-34S in sulphides). Chem Geol 101:53–61

Fleischer VD, Garlick WG, Haldane R (1976) Geology of the Zambian Copper Belt. In: Wolf KH (ed) Handbook of stratabound and stratiform ore deposits, vol 6. Elsevier, New York, pp 223–352

François A (1973) L'extrémité occidentale de l'arc cuprifère shabien. Etude géologique, Bureau d'études géologiques. Gécamines-Exploitation, Likasi, Zaïre, 65 pp

François A (1974) Stratigraphie, tectonique et minéralisations dans l'arc cuprifère du Shaba (République du Zaïre). In: Bartholomé P (ed) Gisements Stratiformes et Provinces Cuprifères. La Société Géologique de Belgique, Liège, pp 79–101

François A (1987) Synthèse géologique sur l'arc cuprifère du Shaba (Rép. Du Zaïre). Centenaire de la Société Belge de Géologie, Liege, pp 15–65

Garlick WG (1961) The syngenetic theory. In: Mendelsohn F (ed) The geology of the Northern Rhodesian Copperbelt. Macdonald, London, pp 146–165

Garlick WG (1965) Criteria for recognition of syngenetic sedimentary mineral deposits and veins formed by their remobilization. Gen. Proc. 8th Commonwealth Min. Metall. Congress, 6, 1393–1418. Proc Australas Inst Min Metall 6:1393–1418

Garlick WG (1981) Sabkhas, slumping, and compaction at Mufulira, Zambia. Econ Geol 76:1817–1847

Garlick WG (1989) Genetic interpretation from ore relations to algal reefs in Zambia and Zaire. In: Boyle RW, Brown AC, Jefferson CW, Jowett EC, Kirkham RV (eds) Sediment-hosted stratiform copper deposits. Geol Ass Canada, Spec Pap 36. Geological Association of Canada, St. John's, pp 471–498

Garlick WG, Brummer JJ (1951) The age of the granites of the northern Rhodesian Copperbelt. Econ Geol 46:478–498

Gray A (1932) The Mufulira copper deposit, Northern Rhodesia. Econ Geol 27:315–343

Gray DR, Gregory RT, Durney DW (1991) Rock-buffered fluid–rock interaction in deformed quartz-rich turbidite sequences, Eastern Australia. J Geophys Res 96:19681–19704

Haest M, Muchez Ph, Dewaele S, Boyce AJ, Av Q, Schneider J (2009) Petrographic, fluid inclusion and isotopic study of the Dikulushi Cu–Ag deposit, Katanga (D.R.C.): implications for exploration. Miner Deposita 44:505–522

Hanson RE, Wardlaw MS, Wilson TJ, Mwale G (1993) U–Pb zircon ages from the Hook granite massif and Mwembeshi dislocation: constraints on Pan-African deformation, plutonism and transcurrent shearing in central Zambia. Precambrian Res 63:189–210

Harrison AG, Thode HG (1957) The kinetic isotope effect in the chemical reduction of sulfate. Trans Faraday Soc 53:1648–1651

Heijlen W, Banks DA, Muchez Ph, Stensgard BM, Yardley BWD (2008) The nature of mineralizing fluids of the Kipushi Zn–Cu deposit, Katanga, Democratic Republic of Congo: quantitative fluid inclusion analysis using laser ablation ICP-MS, and bulk crush-leach methods. Econ Geol 103:1459–1482

Hitzman MW, Beaty DW (1996) The Irish Zn–Pb–(Ba) orefield. Soc Econ Geol Spec Pub 4:112–143

Hitzman MW, Kirkham R, Broughton D, Thorson J, Selley D (2005) The sediment-hosted stratiform copper ore system. Econ Geol 100th Anniversary Volume:609–642

Holser WT (1977) Catastrophic chemical events in the history of the ocean. Nature 267:403–408

Holser WT, Kaplan IR (1966) Isotope geochemistry of sedimentary sulfates. Chem Geol 4:93–155

Hoy LD, Ohmoto H (1989) Constraints for the genesis of redbed associated stratiform Cu deposits from sulphur and carbon mass balance relations. In: Boyle RW, Brown AC, Jefferson CW, Jowett EC, Kirkham RV (eds) Sediment-hosted stratiform copper deposits. Geol Ass Canada, Spec Pap 36. Geological Association of Canada, St. John's, pp 135–149

Hudson JD, Anderson TF (1989) Ocean temperatures and isotopic compositions through time. Trans Roy Soc Edinburgh 80:183–192

Hurtgen MT, Arthur MA, Suits NS, Kaufman AJ (2002) The sulfur isotopic composition of Neoproterozoic seawater sulfate: implications for a snowball Earth? Earth Planet Sci Lett 203:413–429

Hurtgen MT, Arthur MA, Halverson GP (2005) Neoproterozoic sulfur isotopes, the evolution of microbial sulfur species, and the burial efficiency of sulfide as sedimentary pyrite. Geology 33:41–44

Irwin H, Curtis C, Coleman M (1977) Isotopic evidence for source of diagenetic carbonates formed during burial of organic-rich sediments. Nature 269:209–213

Jackson GCA (1932) The geology of the Nchanga district, northern Rhodesia. J Geol Soc Lond 88:443–515

Jackson MPA, Warin ON, Woad GM, Hudec MR (2003) Neoproterozoic allochthonous salt tectonics during the Lufilian orogeny in the Katanga Copperbelt, central Africa. Geol Soc Am Bull 115:314–330

Jacobsen SB, Kaufman AJ (1999) The Sr, C and O isotopic evolution of Neoproterozoic seawater. Chem Geol 161:37–57

John T, Schenk V, Mezger K, Tembo F (2004) Timing and P–T evolution of whiteschist metamorphism in the Lufilian arc-Zambezi belt orogen (Zambia): Implication for the assembly of Gondwana. J Geol 112:71–90

Kampunzu AB, Cailteux J (1999) Tectonic evolution of the Lufilian Arc during Neoproterozoic Pan African orogenesis. Gondwana Res 2:401–421

Kampunzu AB, Cailteux JLH, Kamona AF, Intiomale MM, Melcher F (2009) Sediment-hosted Zn–Pb–Cu deposits in the Central African Copperbelt. Ore Geol Rev 35:263–297

Kelley SP, Fallick AE (1990) High-precision spatially resolved analysis of delta-34-S in sulphides using a laser extraction technique. Geochim Cosmochim Acta 54:883–888

Kenis I, Muchez Ph, Sintubin M, Mansy JL, Lacquement F (2000) The use of a combined structural, stable isotope and fluid inclusion study to constrain the kinematic history at northern Variscan front zone (Bettrechnies, northern France). J Struct Geol 22:589–602

Key RM, Liyungu AK, Njamu FM, Somwe V, Banda J, Mosley PN, Armstrong RA (2001) The western arm of the Lufilian Arc in NW Zambia and its potential for copper mineralization. J Afr Earth Sci 33:503–528

Kirkham RV (1989) Distribution, settings and genesis of sediment-hosted stratiform copper deposits. In: Boyle RW, Brown AC, Jefferson CW, Jowett EC, Kirkham RV (eds) Sediment-hosted stratiform copper deposits. Geol Ass Canada, Spec Pap 36. Geological Association of Canada, St. John's, pp 3–38

Kiyosu Y, Krouse HR (1990) The role of organic acid in the abiogenic reduction of sulfate and the sulfur isotope effect. Geochem J 24:21–27

Kohn MJ, Riciputi LR, Stakes D, Orange DL (1998) Sulfur isotope variability in biogenic pyrite: reflections of heterogeneous bacterial colonization? Am Mineral 83:1454–1468

Land LS (1983) The application of stable isotopes to studies of the origin of dolomite and to problems of diagenesis of clastic sediments. In: Arthur MA (ed) Stable isotopes in sedimentary geology. Society of Economic Paleontologists and Mineralogists, Tulsa, pp 4.1–4.22

Lefebvre JJ (1989) Depositional environment of copper–cobalt mineralization in the Katangan sediments of southeast Shaba. In: Boyle RW, Brown AC, Jefferson CW, Jowett EC, Kirkham RV (eds) Sediment-hosted stratiform copper deposits. Geol Ass Canada, Spec Pap 36. Geological Association of Canada, St. John's, pp 401–426

Lerouge C, Cocherie A, Cailteux J, Kampunzu AB, Breton J, Gilles C, Milési J-P (2004) Preliminary U–Th–U electron microprobe dating of monazite: chronological constraints on the genesis of the Luiswishi Cu–Co–U ore deposit, D.R. Congo. Proceedings of the Geosciences Africa 2004, University of the Witwatersrand, Johannesburg, South Africa, Abstract vol. 1, pp 382–383

Lerouge C, Cailteux J, Kampunzu AB, Milesi JP, Fléhoc C (2005) Sulphur isotope constraints on formation conditions of the Luiswishi ore deposit, Democratic Republic of Congo (DRC). J Afr Earth Sci 42:173–182

Lindsay JF, Kruse PD, Green OR, Hawkins E, Brasier MD, Cartlidge J, Corfield RM (2005) The Neoproterozoic–Cambrian record in Australia: a stable isotope study. Precambrian Res 143:113–133

Machel HG (1987a) Saddle dolomite as a by-product of chemical compaction and thermochemical sulfate reduction. Geology 15:936–940

Machel HG (1987b) Some aspects of diagenetic sulphate-hydrocarbon redox-reactions. In: Marshall JD (ed) Diagenesis of sedimentary sequences. Geol Soc Spec Pub 36. Geological Society, London, pp 15–28

Machel HG (2001) Bacterial and thermochemical sulfate reduction in diagenetic settings—old and new insights. Sediment Geol 140:143–175

Machel HG, Foght J (2000) Products and depth limits of microbial activity in petroliferous subsurface settings. In: Riding RE, Awramik SM (eds) Microbial sediments. Springer, Berlin, pp 105–120

Machel HG, Krouse HR, Sassen R (1995) Products and distinguishing criteria of bacterial and thermochemical sulfate reduction. Appl Geochem 10:373–389

Macqueen RW, Powell TG (1983) Organic geochemistry of the Pine Point lead–zinc ore field and region, Northwest Territories, Canada. Econ Geol 78:1–25

Marquer D, Burkhard M (1992) Fluid circulation, progressive deformation and mass-transfer processes in the upper crust: the example of basement-cover relationship in the External Crystalline Massifs, Switzerland. J Struct Geol 14:1047–1057

Master S, Rainaud C, Armstrong RA, Phillips D, Robb LJ (2005) Provenance ages of the Neoproterozoic Katanga Supergroup (Central African Copperbelt), with implications for basin evolution. J Afr Earth Sci 42:41–60

McGowan RR, Roberts S, Foster RP, Boyce AJ, Coller D (2003) Origin of the copper–cobalt deposits of the Zambian Copperbelt: an epigenetic view from Nchanga. Geology 31:494–500

McGowan RR, Roberts S, Boyce AJ (2006) Origin of the Nchanga copper–cobalt deposits of the Zambian Copperbelt. Miner Deposita 40:617–638

Mendelsohn F (1961a) Metamorphism. In: Mendelsohn F (ed) The geology of the Northern Rhodesian Copperbelt. Macdonald, London, pp 106–116

Mendelsohn F (1961b) Ore genesis: summary of the evidence. In: Mendelsohn F (ed) The geology of the Northern Rhodesian Copperbelt. Macdonald, London, pp 130–146

Misra KC (2000) Understanding mineral deposits. Kluwer Academic, Dordrecht, 845 pp

Molak B (1995) Some structural and petrological aspects of the Cu (Co) mineralization in the Copperbelt and northwestern provinces of Zambia. Tervuren, Belgium, Royal Museum of Central Africa. Ann Sci Géol 101:95–102

Mougin P, Lamoureux-Var V, Bariteau A, Huc AY (2007) Thermodynamics of thermochemical sulphate reduction. J Petrol Sci Eng 58:413–427

Muchez Ph, Slobodnik M, Viaene W, Keppens E (1995) Geochemical constraints on the origin and migration of palaeofluids at the northern margin of the Variscan foreland, southern Belgium. Sediment Geol 96:191–200

Muchez Ph, Brems D, El Desouky H, Dewaele S, Haest M, Vanderhaegen P, Heijlen W, Mukumba W (2007) Base metal ore deposit evolution and geodynamics in the Central African Copperbelt. In: Andrew CJ et al (eds) Digging deeper—proceedings of the 9th Biennial SGA Meeting. Irish Association for Economic Geology, Dublin, pp 209–212

Muchez Ph, Vanderhaeghen P, El Desouky H, Schneider J, Boyce A, Dewaele S, Cailteux J (2008) Anhydrite pseudomorphs and the origin of stratiform Cu–Co ores in the Katangan Copperbelt (Democratic Republic of Congo). Miner Deposita 43:575–589

Müller G (1967) Diagenesis in argillaceous sediments. In: Larsen G, Chilingar GU (eds) Diagenesis in sediments, developments in sedimentology 8. Elsevier, Amsterdam, pp 127–178

Ngoyi K, Liégeois J-P, Demaiffe D, Dumont P (1991) Age tardiubendien (Protérozoïque inférieur) des dômes granitiques de l'arc cuprifère zaïro-zambien. Compte Rendu de l'Académie des Sciences Paris 313:83–89

Nielsen P, Swennen R, Keppens E (1994) Multiple-step recrystallization within massive ancient dolomite units: an example from the Dinantian of Belgium. Sedimentology 41:567–584

Ohmoto H (1986) Stable isotope geochemistry of ore deposits. In: Valley JW, Taylor HP, O'Neil JR (eds) Stable isotopes in high temperature geological processes. Reviews in mineralogy 16. Mineralogical Society of America, Chantilly, pp 491–559

O'Neil JR, Clayton RN, Mayeda TK (1969) Oxygen isotope fractionation in divalent metal carbonates. J Chem Phys 51:5547–5558

Porada H (1989) Pan-African rifting and orogenesis in southern to equatorial Africa and eastern Brazil. Precambrian Res 44:103–136

Porada H, Berhorst V (2000) Towards a new understanding of the Neoproterozoic–Early Palaeozoic Lufilian and northern Zambezi belts in Zambia and the Democratic Republic of Congo. J Afr Earth Sci 30:727–771

Rainaud C, Master S, Armstrong RA, Phillips D, Robb LJ (2005) Monazite dating and ^{40}Ar–^{39}Ar thermochronology of metamorphic events in the Central African Copperbelt during the Pan-African Lufilian Orogeny. J Afr Earth Sci 42:183–199

Rosenbaum J, Sheppard SM (1986) An isotopic study of siderites, dolomites and ankerites at high temperatures. Geochim Cosmochim Acta 50:1147–1150

Schwartz GM (1934) Paragenesis of the oxidized ores of copper. Econ Geol 29:55–75

Selley D, Broughton D, Scott R, Hitzman M, Bull S, Large R, McGoldrick P, Croaker M, Pollington N, Barra F (2005) A new look at the geology of the Zambian Copperbelt. Econ Geol 100th Anniversary Volume:965–1000

Sheppard SMF (1986) Characterization and isotopic variations in natural waters. In: Valley JW, Taylor HP Jr, O'Neil JR (eds) Stable isotopes in high temperature geological processes. Mineralogical Society of America, Washington, D.C., 570 pp

Smith TM, Dorobek SL (1993) Alteration of early-formed dolomite during shallow to deep burial: Mississippian Mission Canyon Formation, central to southwestern Montana. Geol Soc Am Bull 105:1389–1399

Sweeney MA, Binda PL (1989) The role of diagenesis in the formation of the Konkola Cu–Co ore-body of the Zambian Copperbelt. In: Boyle RW, Brown AC, Jefferson CW, Jowett EC, Kirkham RV (eds) Sediment-hosted stratiform copper deposits. Geol Ass Canada, Spec Pap 36. Geological Association of Canada, St. John's, pp 499–518

Sweeney MA, Binda PL (1994) Some constraints on the formation of the Zambian Copperbelt deposits. J Afr Earth Sci 19:303–313

Sweeney MA, Turner P, Vaughan DJ (1986) Stable isotope and geochemical studies of the role of early diagenesis in ore formation, Konkola basin, Zambian Copperbelt. Econ Geol 81:1838–1852

Sweeney MA, Binda PL, Vaughn DJ (1991) Genesis of the ores of the Zambian Copperbelt. Ore Geol Rev 6:51–76

Unrug R (1988) Mineralisation controls and source of metals in the Lufilian Fold Belt, Shaba (Zaire), Zambia and Angola. Econ Geol 83:1247–1258

Veizer J, Hoefs J (1976) The nature of $^{18}O/^{16}O$ and $^{13}C/^{12}C$ secular trends in sedimentary carbonate rocks. Geochim Cosmochim Acta 40:1387–1395

Verhaert G, Muchez Ph, Keppens E, Sintubin M (2009) Fluid impact and spatial and temporal evolution of normal faulting in limestones. A case study in the Burdur-Isparta region (SW Turkey). Geol Belg 12:59–73

Wachter E, Hayes JM (1985) Exchange of oxygen isotopes in carbon-dioxide–phosphoric acid systems. Chem Geol 52:365–374

Wagner T, Boyce AJ (2006) Pyrite metamorphism in the Devonian Hunsrück Slate of Germany: insights from laser microprobe sulfur isotope analysis and thermodynamic modelling. Am J Sci 306:525–552

Wagner T, Okrusch M, Weyer S, Lorenz J, Lahaye Y, Taubald H, Schmitt RT (2010) The role of the Kupferschiefer in the formation of hydrothermal base metal mineralization in the Spessart ore district, Germany: insight from detailed sulfur isotope studies. Miner Deposita 45:217–239

Wendorff M (2000) Genetic aspects of the Katangan megabreccias: Neoproterozoic of Central Africa. J Afr Earth Sci 30:703–715

Wendorff M (2005) Evolution of Neoproterozoic–Lower Palaeozoic Lufilian arc, Central Africa: a new model based on syntectonic conglomerates. J Geol Soc Lond 162:5–8